PCCP

ROYAL SOCIETY OF CHEMISTRY

PAPER

View Article Online
View Journal | View Issue

Cite this: *Phys. Chem. Chem. Phys.*, 2025, **27**, 11762

Substrate charge transfer drives the adsorption site of metal-phthalocyanines and porphyrins on coinage metal surfaces†

Silvia Carlotto, [ab] Iulia Cojocariu, [cd] Vitaliy Feyer, [ef] Luca Schio, [g] Luca Floreano [g] and Maurizio Casarin *[a]

Received 25th April 2025,
Accepted 15th May 2025

DOI: 10.1039/d5cp01576f

rsc.li/pccp

The Frontier electronic structure of tetraphenylporphyrinato (TPP^{2-}) and phthalocyaninato (Pc^{2-}) square planar transition metal complexes (MTPP and MPc; M = V, Cr, Mn, Fe, Co, Ni, Cu, and Zn) has been revisited through DFT calculations. The different ground state symmetry and spin multiplicity between MPc and MTPP of the same M is shown to originate from the different Pc^{2-} and TPP^{2-} ligand field, stronger in the former ligand than in the latter. The corresponding spatial localization and symmetry of the unoccupied molecular orbitals postulate unescapable geometric constraints to their overlap with the electron cloud of a crystalline metal surface. From comparison with literature experimental evidence, we show that the adsorption geometry (atomic site and azimuthal orientation) of MTPPs and MPcs on the low index crystal planes of coinage metals (CM = Au, Ag, Cu) may be predicted when two conditions are satisfied: (i) evidence of a surface → adsorbate charge transfer, (ii) absence of significant distortion of the macrocycle upon adsorption. In this regard, the overall susceptibility to charge transfer is determined by the strength of the molecular ligand field (*i.e.*, charge transfer to MPc is more favoured than to MTPP) and inversely linked to the electronegativity of the surface atoms (being Au the most inert CM substrate thanks to its highest electronegativity).

[a] *Dipartimento di Scienze Chimiche, Università degli Studi di Padova, Via Francesco Marzolo 1, 35131 Padova, Italy. E-mail: maurizio.casarin@unipd.it*
[b] *CNR – ICMATE, Via Francesco Marzolo 1, 35131 Padova, Italy*
[c] *Dipartimento di Fisica, Università degli Studi di Trieste, Via Alfonso Valerio 2, 34127 Trieste, Italy*
[d] *Elettra-Sincrotrone, S.C.p.A., Basovizza S.S. 14 – km 163.5, 34149 Trieste, Italy*
[e] *Forschungszentrum Jülich GmbH, Peter Grünberg Institute (PGI-6), Leo-Brandt-Strabe, 52428 Jülich, Germany*
[f] *Duisburg-Essen University, Department of Physics and Center for Nanointegration Duisburg-Essen (CENIDE), 47048 Duisburg, Germany*
[g] *IOM – CNR, Lab. TASC, Basovizza S.S. 14, km 163.5, 34149 Trieste, Italy*

† Electronic supplementary information (ESI) available: Frontier electronic structure of MTPP and MPc (M = V, Cr, Mn, Fe, Co, Ni, Cu, and Zn) isolated complexes. Optimized coordinates of Py, i-Ind, H_2P, H_2Pz, H_2TPP, H_2Pc, P^{2-}, Pz^{2-}, TPP^{2-}, and Pc^{2-} in Tables S1–S10; optimized coordinates of MTPP and MPc in Tables S13, S16–S24, S27, S28, S30, S31, S33, and S34; optimized coordinates of $CoPc^+$, $NiPc^+$, $CuPc^+$, and $ZnPc^+$ in Tables S25, S29, S32, and S35; H_2TPP, H_2Pc, MTPP, and MPc TSIEs in Table S11; MTPP and MPc optimized/experimental M–N^{Py} bond lengths in Table S12; MTPP and MPc GS terms and low-lying excited state terms sharing the same GS spin multiplicity in Table S14; MTPP and MPc TSEAs in Table S15; theoretical/experimental ν values of the IR-active $22e_u$ vibrational mode of MPc and MPc^+ (M = Co, Ni, Cu, and Zn) in Table S25; selected internuclear distances (Å) in: D_{2h} H_2P and H_2Pz (Fig. S1); D_{2h} H_2TPP and H_2Pc (Fig. S2); D_{4h} P^{2-} and Pz^{2-} (Fig. S3); D_{4h} TPP^{2-} and Pc^{2-} (Fig. S4); energy position of H_2P, H_2TPP, H_2Pc, and H_2Pz GS FMOs (Fig. S5); 3D CPs of the Py and i-Ind HOMOs (Fig. S6); 3D CP of the i-IND $1a_2$ π MO (Fig. S7); 3D CPs of H_2P FMOs generated by the $1a_2$ Py HOMO (Fig. S8); 3D CPs of low-lying H_2P π MOs (Fig. S9); parenthood between ^{pmc}π and ^{pmc}π* Frontier MOs upon D_{2h} → D_{4h} switching (Fig. S10); 3D CPs of low-lying TPP^{2-} and Pc^{2-} π* MOs (Fig. S11); superposition of the CoPc ($^2A_{1g}$) and $CoPc^+$ ($^3A_{1u}$), NiPc ($^1A_{1g}$) and $NiPc^+$ ($^2A_{1u}$), CuPc ($^2B_{1g}$) and $CuPc^+$ ($^3B_{1u}$), ZnPc ($^1A_{1g}$) and $ZnPc^+$ ($^2A_{1u}$) otpimized structures in Fig. S12; schematic representation of the ^{S}CM *ns* AOs SALCs in Fig. S13–S17. See DOI: https://doi.org/10.1039/d5cp01576f

1. Introduction

The control of the interfacial structure between organic/metalorganic molecular layers and the underlying substrate is crucial to reproducing the functional properties of the organic/metalorganic component in surface-supported devices. Even tiny alterations of the interface structure may severely modify the behavior of the overlayer both at the supramolecular and the single-molecule level, thus generating significant changes independently of the investigated property (mechanical,[1] electronic,[2–4] optical,[5,6] magnetic[7,8]) or the application field (sensing, catalysis, light-to-energy conversion, molecular electronics, nonlinear optics, spintronics). Among surface-supported layers, those made up of transition-metal complexes of porphyrin-related molecules (see the upper panel of Fig. 1)‡ are particularly relevant because of the pivotal role played by porphyrins not only in fundamental biological processes such as oxygen transport and storage, the photosynthesis, and the electron transport during cellular respiration

‡ Porphine (H_2P) is an aromatic ($4n + 2$; $n = 4$ for the shortest cyclic path), heterocyclic, organic compound consisting of four pyrrole fragments held together by as many methylidene bridges, which makes it the simplest tetrapyrrole ($C_{20}H_{14}N_4$). Because of the H_2P low solubility, the interest for the pristine molecule is mainly theoretical. Substituted porphines correspond to porphyrins; *meso*-tetraphenylporphyrin (H_2TPP) is the most common.[9] The acronym herein used for M complexes of H_2TPP is MTPP.

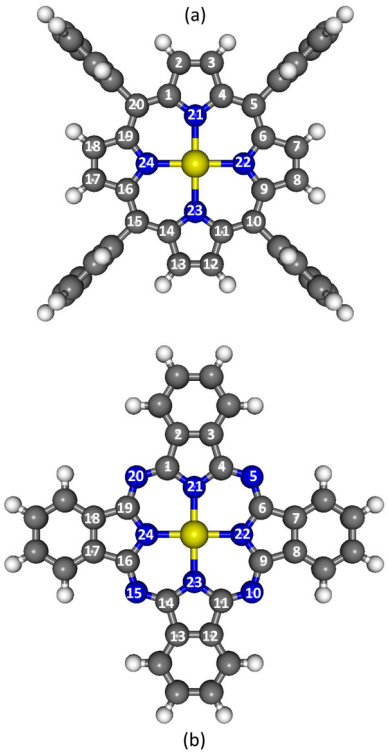

Fig. 1 Idealized representation of D_{4h} MTPP and MPc isolated molecules. White, gray, blue, and yellow spheres are representative of H, C, N, and M atoms, respectively. In the adopted framework, M lies in the origin O of the coordinate axes, M–N^{Py} bonds are aligned with OX and OY axes, and the σ_h plane corresponds to the XY plane. The atom numbering adopted for the planar, aromatic macrocycle core (pmc) is that recommended by IUPAC.

and photosynthesis,[10,11] but also in technological fields ranging from electronics[12] to solar cells,[13] and sensors,[14] thus justifying the cross-disciplinary interest towards them and motivation to develop new porphyrin-like species, whose electronic and optical properties may be tuned through molecular engineering.[15–23]

Unlike porphyrins, neither the H_2Pc free-base nor MPc complexes (see the lower panel of Fig. 1) are present in Nature. Nonetheless, they have been attracting a growing interdisciplinary interest[20,24–30] since their synthesis by serendipity at the end of the twenties of the last century[31–39] because their technological potential spans a huge range of applications including catalysts,[26] dyestuffs for textiles and inks, intrinsic semiconductors, chemical sensors, organic light-emitting diodes, organic photovoltaic cells, thin-film transistors, materials for nonlinear optics, spintronics, and laser recording as well.[40–43]

From a structural point of view, isolated MTPPs are usually characterized by a planar, aromatic macrocycle core (hereafter, pmc) consisting of four Py-like rings held together by four methine groups in *m* positions (see the upper panel of Fig. 1 where the adopted atom numbering is that recommended by IUPAC and *m* sites correspond to the 5, 10, 15, and 20 positions). Additionally, 1, 4, 6, 9, 11, 14, 16, and 19 (2, 3, 7, 8, 12, 13, 17, and 18) positions are commonly referred to as α-positions (β-positions). Similarly to MTPPs, isolated MPcs consist of four i-Ind (a benzene ring fused with Py) fragments held together by four aza-nitrogen atoms occupying the pmc *m* positions (see the lower panel of Fig. 1 where the adopted atom numbering is again the one recommended by IUPAC).

Upon moving from the isolated to the adsorbed species, the coordinative arrangements of the on-surface stabilized arrays of M ions may be exploited to boost free molecules' peculiar properties,[44,45] to stabilize M in unusual spin and oxidation states[46–53] or, in wider terms, to control and tune their chemical reactivity.[54–58] As such, a crucial issue is the pmc adsorption site, usually determined by combining the outcomes of STM measurements with the results of expensive and time-consuming quantum mechanical calculations, commonly based on DFT.[20,23] However, DFT-based numerical experiments have often been restricted to the generation of phenomenological descriptions rather than exploring in detail the anchoring configurations of the adsorbate–substrate pair.[20,23]

Li *et al.*[25] tackled the single-molecule chemistry of MPcs on the (111) surface of group 11 elements (CM) by combining first-principles simulations with STM, which, besides information about the local adsorption geometry and the electronic properties of chemisorbed MPcs, was exploited to carry out the so-called single-molecule surgery to control the Kondo effect[59] at the MPc/CM(111) interface. Nevertheless, the DFT numerical experiments carried out by Li *et al.*[25] did not provide any atomistic modeling of the MPc–CM(111) anchoring configuration to explain, for instance, why the chemisorption site of the same MPc may be different on the (111) surface of diverse CM or why the chemisorption site of diverse MPcs may be different on the (111) surface of the same group 11 element. In this regard, we recently proposed convincing modeling of the NiTPP anchoring to the Cu(100) surface, as well as an atomistic view of the Cu(100) → NiTPP charge transfer taking place at the interface.[60] Starting from the experimentally reported Ni^{II} (d^8) → Ni^{I} (d^9) reduction at the interface,[61] the NiTPP chemisorption site and the molecular orientation on Cu(100) can be unequivocally assigned as confirmed by the structural outcomes of PED measurements.[60] The charge transfer from specific substrate atoms to specific adsorbate atoms follows the spatial superposition of the symmetry-allowed substrate and molecular orbitals, according to the matching of the intramolecular atomic structure with the substrate lattice spacing. More specifically, symmetry and geometry arguments made it practically unessential to carry out costly numerical experiments to assess the chemisorption configuration. Our analysis relied on identifying the NiTPP lowest-lying unoccupied MOs and the SALCs of the substrate topmost atoms (^{S}Cu) 4s AOs involved in the charge transfer process. The latter point implies that each ^{S}Cu participates in the adsorbate/substrate interaction, with its single electron occupying its 4s AO, while the electrons of the completely occupied 3d shell are simple bystanders.

The use of MTPP and MPc symmetry, orbitals, and spectra[62] coupled with a descriptor able to provide information about the different nobleness of group 11 elements turned out to be Hobson's choice to set up a protocol able to provide a semi-quantitative modeling of the ^{S}CM → MTPP/MPc charge transfer when MTPP/MPc complexes are chemisorbed on CM (100), (110), and (111) surfaces. In this regard, it is notable that Kepp thoroughly investigated the chemical causes of M nobleness a few years ago.[63] More specifically, he considered all the group 10 and 11 elements as well as the heaviest element of group 12 (Hg), and he tested 12 different descriptors, including, by the way, the d-band center energy of the solid, the first IE and the EA, the Pauling electronegativity χ,[64] the bulk polycrystalline M work function, the relativistic s-shell contraction, the oxophilicity of M, and the cohesive free energy (free energy of atomization) of the bulk M state, to conclude that the M's χ explains best the M nobleness.[63] The noblest metal is then Au, whose high χ (2.54 Pauling's units, the highest among metals)[65,66] is determined by concurrent effects such as the high effective nuclear charge and the contraction of the half-filled 6s AO.[67] As such, Pyykkö[67–69] pointed out that the ratio of relativistic and nonrelativistic 6s shell radii in the atomic GS of the elements with the atomic number Z ranging from 55 to 100 has a marked minimum for Z = 79, and there is often talk of the "gold maximum" of relativistic effects in group 11, whose elements are all characterized by the electronic configuration $d^{10}s^{1}$.[65]

Even though the high $^{Au}\chi$[65,66] provides a rationale for understanding the inertness of gold surfaces independently of Miller indices and chemisorption sites' local symmetry, genuine unpublished results and literature data will be compared with the provisions of the proposed approach in the forthcoming discussion. In more detail: (i) results on the Frontier electronic structure of isolated MTPP and MPc (M = V, Cr, Mn, Fe, Co, Ni, Cu, Zn), critically revisited and compared with literature experimental and theoretical evidence in the ESI,† are summarized in Paragraph 3.1; (ii) clean, bulk-terminated CM (100), (110), and (111) surfaces have been considered in Paragraph 3.2 by focusing on the local symmetry properties of their most common chemisorption sites; (iii) the proposed approach is applied in Paragraph 3.3 to selected MTPP/CM and MPc/CM interfaces (sub-Paragraphs 3.3.1–3.3.5) representing as many case studies.

2. Computational details

The GS electronic configurations of MPcs (Z^{M} = 25–30) have been thoroughly investigated by multireference electronic structure methods in the past.[70] Nonetheless, the GS structural and electronic properties of free MTPP and MPc complexes (Z^{M} = 23–30) have been re-investigated herein at the DFT level by exploiting the ADF package.[71] ADF numerical experiments have been carried out within the assumption of an idealized D_{4h} symmetry[72] (see Fig. 1) and by running nonrelativistic, spin-polarized calculations with generalized gradient corrections self-consistently included through the BP86 formula.[73,74] A triple-ζ with a polarization function Slater-type basis set has been adopted for all the atoms; moreover, the $(1s–2p)^{M}$, $1s^{N}$, and $1s^{C}$ cores have been kept frozen throughout the calculations.§¶ IEs and EAs of valence MOs have been estimated through spin-polarized TS calculations.[75] The adopted set-up allowed the comparison of ADF results with homogeneous theoretical outcomes pertinent to CoTPP,[51,52,56,76] NiTPP,[52,53,60] CuTPP,[77,78] MPc (M = V,[79–81] Cr,[79] Mn,[79] Fe,[79] and Cu[81–84]). In a few selected cases (*vide infra*), further numerical experiments have been carried out by employing the same ADF package, the same basis sets, and a hybrid functional (B3LYP),[85] incorporating a portion of exact exchange (20%) from Hartree–Fock theory.

3. Results and discussion

3.1 Isolated MTPP and MPc

The square planar arrangement of M^{II} ions in both MTPP and MPc lifts the five-fold degeneracy of the M 3d AOs to generate, within the assumption of a local D_{4h} symmetry[72] and the framework adopted in Fig. 1, five spin-up orbitals ($SO^{\uparrow}$) of symmetry a_{1g} (z^2), b_{1g} (x^2–y^2), b_{2g} (xy), e_g (xz, yz) and as many $SO^{\downarrow}$ of the same symmetry. These SOs may be grouped in parallel ($\parallel$) and perpendicular ($\perp$) $^{\pi}t_{2g}$-like ($^{\pi}_{\parallel}b_{2g}$ + $^{\pi}e_g$) SOs and $^{\sigma}e_g$-like SOs ($^{\sigma}a_{1g}$ + $^{\sigma}b_{1g}$) by exploiting the parenthood between D_{4h} and O_h complexes.[72] It is noteworthy that the M $^{\sigma}e_g$-like $^{\sigma}b_{1g}^{\uparrow}$ SO, antibonding in nature with respect to the $M–N^{Py}$ σ interaction, is certainly occupied in the $3d^5$ HS MnTPP,[86] $3d^9$ CuTPP[78,87,88] and CuPc,[81–84,89–91] and $3d^{10}$ ZnTPP and ZnPc complexes;[90–92] moreover, only the closed-shell ZnTPP and ZnPc have no vacancy in the Zn 3d-based SOs. Additionally, the Pc^{2-} ligand field is experimentally and theoretically found slightly stronger than the TPP^{2-} one[78,86,93] (see Section ESI.1 of the ESI†). This last evidence scarcely affects MTPP and MPc complexes whose $^{\pi}t_{2g}^{\uparrow}$-/$^{\pi}t_{2g}^{\downarrow}$-like SOs are filled, and the $^2A_{1g}$ (Co^{II}, $3d^7$), $^1A_{1g}$ (Ni^{II}, $3d^8$), $^2B_{1g}$ (Cu^{II}, $3d^9$), and $^1A_{1g}$ (Zn^{II}, $3d^{10}$) GSs uniquely determined;‖ however, it could be relevant in lighter complexes, whose GS electronic terms are still debated[79,94] and could be different upon moving from MTPP to MPc.[78,86,93]

As mentioned in the Introduction, the frontier electronic structure of MTPP and MPc isolated complexes has been critically revisited and thoroughly compared with literature data in the ESI† (Section ESI.2). The relevant results of such a review will be briefly discussed by referring to Tables 1, 2, and Fig. 2.

Starting from the occupied FMOs and, more specifically, from the $^{pmc}\pi$ ones; *i.e.*, the H_2TPP $13b_{1u}$ and $10a_u$ FMOs, the

§ ADF outcomes about isolated MTPP and MPc are compared with the results of the literature in the ESI.†

¶ Throughout the paper, the MO numbering corresponds to all-electron calculations independently of adopting the frozen core approximation.

‖ Both Co^{II} ($3d^7$) and Ni^{II} ($3d^8$) complexes are characterized by a low-spin (LS) state with $S = \frac{1}{2}$ and $S = 0$, respectively (see Section ESI.2, ESI†).

Table 1 H_2TPP (H_2Pc) TSIEs (eV) of the $10a_u$ and $13b_{1u}$ ($7b_{1u}$ and $4a_u$) MOs.¶ MTPP and MPc TSIEs of the M-based $^{\sigma}a_{1g}$, $^{\sigma}b_{1g}$, $^{\pi}b_{2g}$, $^{\pi}e_g$, and pmc-based $^{\pi}a_{1u}$ and $^{\pi}a_{2u}$ SOs. Values of the lowest TSIE are in bold[a]

	$^{\sigma}a_{1g}$	$^{\sigma}b_{1g}$	$^{\pi}b_{2g}$	$^{\pi}e_g$	$a_{1u}{}^{\downarrow}$	$a_{2u}{}^{\downarrow}$
H_2TPP	—	—	—	—	6.77 ($10a_u$)	**6.48** ($13b_{1u}$)
H_2Pc	—	—	—	—	**6.57** ($4a_u$)	7.74 ($7b_{1u}$)
VTPP	$6.29^{\uparrow}$	—	$6.37^{\uparrow}$	**5.69**$^{\uparrow}$	6.72	6.50
VPc	$6.74^{\uparrow}$	—	$6.59^{\uparrow}$	**6.17**$^{\uparrow}$	6.49	7.98
CrTPP	$7.28^{\uparrow}$	—	$7.69^{\uparrow}$	$6.63^{\uparrow}$	6.69	**6.54**
CrPc	$7.73^{\uparrow}$	—	$7.44^{\uparrow}$	$7.03^{\uparrow}$	**6.50**	7.99
MnTPP	$9.61^{\uparrow}$	**5.88**$^{\uparrow}$	$9.49^{\uparrow}$	$10.53^{\uparrow}$	6.55	6.36
MnPc	$8.40^{\uparrow}$	—	$9.33^{\uparrow}$	**5.99**$^{\downarrow}$	6.57	8.00
FeTPP	**6.18**$^{\downarrow}$	—	$6.45^{\downarrow}$	$7.08^{\uparrow}$	6.70	6.57
FePc	$6.65^{\downarrow}$	—	$6.77^{\downarrow}$	$8.63^{\uparrow}$	**6.51**	8.01
CoTPP	$8.94^{\uparrow}$	—	$7.60^{\downarrow}$	$6.85^{\downarrow}$	6.69	**6.60**
CoPc	$9.14^{\uparrow}$	—	$7.62^{\downarrow}$	$7.32^{\downarrow}$	**6.54**	8.01
NiTPP	$7.65^{\downarrow}$	—	$8.63^{\downarrow}$	$7.03^{\downarrow}$	6.70	**6.62**
NiPc	$8.36^{\downarrow}$	—	$8.03^{\downarrow}$	$7.47^{\downarrow}$	**6.55**	8.03
CuTPP	$9.72^{\downarrow}$	$6.95^{\uparrow}$	$9.39^{\downarrow}$	$9.64^{\downarrow}$	6.72	**6.55**
CuPc	$9.17^{\downarrow}$	$7.28^{\uparrow}$	$8.08^{\downarrow}$	$7.77^{\downarrow}$	**6.56**	8.01
ZnTPP					6.72	**6.54**
ZnPc					**6.55**	7.98

[a] HS MnTPP TSIE calculations have been run by adopting the B3LYP functional.

H_2Pc $7b_{1u}$ and $4a_u$ FMOs, the MTPP $12a_{2u}$ and $2a_{1u}$ FMOs, and the MPc $6a_{2u}$ and $2a_{1u}$ FMOs, the following statements hold: (i) TSIEs of the $12a_{2u}$ ($13b_{1u}$ in H_2TPP)** FMO are very similar along the whole TPP series (the IE range they cover is less than 0.2 eV wide; see Table 1 and Fig. 2, where the MnTPP $12a_{2u}$ FMO TSIE is not considered because evaluated by running B3LYP-based TS calculations (see Section ESI.2, ESI†)); (ii) TSIEs of the $6a_{2u}$ ($7b_{1u}$ in H_2Pc)** FMO are very similar along the whole Pc series and vary between 7.74 and 8.01 eV (see Table 1 and Fig. 2); (iii) nodal properties of the $2a_{1u}$ MO (the $10a_u$ FMO in H_2TPP and the $4a_u$ FMO in H_2Pc)** make corresponding TSIEs very similar to each other; the $|\Delta TSIE|$ between the $12a_{2u}$ and $2a_{1u}$ ($10a_u$ and $13b_{1u}$ in H_2TPP)** FMOs is tiny ($\sim$0.2 eV) in MTPP; in addition, the $\Delta TSIE$ between the $6a_{2u}$ and the $2a_{1u}$ ($7b_{1u}$ and $4a_u$ in H_2Pc)** FMOs is rather constant ($\sim$1.5 eV) in MPc. Moving to the M 3d-based occupied FMOs, photoemission processes involving an M 3d-based MO and lying at the lowest IE are limited to VTPP, FeTPP (TSIEs of MnTPP FMOs have been computed by running B3LYP-based TS calculations; see Section ESI.2, ESI†), VPc, and MnPc.

Data on unoccupied MTPP and MPc FMOs are, for this contribution, much more interesting to be jointly considered. Let us start from the $^{pmc}\pi^*$ FMOs; *i.e.*, the quasi degenerate $12b_{2g}/12b_{3g}$ and the $11a_u$ FMOs in H_2TPP, the quasi degenerate $6b_{2g}/6_{3g}$ and the $5a_u$ FMOs in H_2Pc, and the e_g and b_{1u} FMOs in MTPP and MPc (see Table 2 and Fig. 2). Similarly to the free H_2TPP and H_2Pc species, the $^{pmc}e_g$ and $^{pmc}b_{1u}$ MPc TSEAs lye deeper in energy than the MTPP ones; moreover, the MPc $^{pmc}b_{1u}$ TSEAs (see Table 2 and Fig. 2) and, separately, the MTPP $^{pmc}b_{1u}$ TSEAs are scarcely affected by the presence of different M along the two series because of the symmetry forbidden participation of the M AOs to the b_{1u} MOs. Moving to the M 3d-based unoccupied FMOs, two things are particularly relevant: (i) both in MTPP and MPc, the largest EA corresponds to an M 3d-based unoccupied FMO only in V ($^{\pi}e_g^{\uparrow}$) and Co ($^{\sigma}a_{1g}^{\downarrow}$) complexes (see Table 2 and Fig. 2); (ii) among the MTPP complexes, CoTPP is the only one with both $^{\sigma}e_g$-like FMOs (the $^{\sigma}a_{1g}^{\downarrow}$ and $^{\sigma}b_{1g}^{\uparrow}$ SOs) able to be involved in a charge transfer processes (see Table 2 and Fig. 2).

3.2 Bulk-terminated CM surfaces

Copper, silver, and gold share the same space group 225 ($Fm\bar{3}m$) and the cubic-close-packed (ccp) crystal structure; corresponding cell parameters are $a = b = c$ (^{Cu}a = 3.61496 Å; ^{Ag}a = 4.0853 Å; ^{Au}a = 4.0782 Å) and $\alpha = \beta = \gamma = 90°$.[95] A schematic representation of the two outermost layers of the bulk terminated CM(100) and CM(110) surfaces is displayed in Fig. 3,†† which also includes a top view of the three CM(111) unreconstructed topmost layers (high-symmetry chemisorption sites are also pinpointed in the figure).

The inspection of Fig. 3 reveals that local symmetry properties of these sites are quite different. More specifically, both CM(100) T and H sites are characterized by a local fourfold symmetry (C_4), reduced to a local C_2 symmetry when the B site is considered; (ii) no CM(110) chemisorption site (T, H, SB, and LB) exceeds a local C_2 symmetry; (iii) CM(111) T, H, and B sites have a local C_6, C_3, and C_2 symmetry, respectively. Incidentally, details of possible surface reconstructions, such as those affecting all the Au low-index planes, are neglected herein.‡‡ More generally, an interacting adsorbate (*i.e.*, subject to charge transfer) will locally disrupt the collective (periodic) surface properties, and the frontier orbitals of the ^{S}CM atoms underneath the adsorbate will recover their atomic-like symmetry.

Coming back to the topmost layer of the bulk terminated CM surfaces, the single *n*s AO (n = 4, 5, and 6 for Cu, Ag, and Au, respectively) localized on a ^{S}CM T site ($^{S}_{T}$CM), independently of the local symmetry, will be a basis for the totally symmetric *ir* (a, in the Schoenflies notation).[72] The situation is a bit more complicated when SALCs of the *n*s AOs centered on chemisorption sites' neighbours are considered: (i) the four SALCs of the *n*s AOs centered on the $^{S}_{T}$CM(100) nnn and $^{S}_{H}$CM(100) nn ($^{S}_{T}CM^{nnn}_{100}$ and $^{S}_{H}CM^{nn}_{100}$, respectively) are bases for the *ir*s a, b, and e (see Fig. S13 and S14 of the ESI†) of the C_4 point group,[72]

** Upon the $D_{2h} \rightarrow D_{4h}$ switching, the following correlations hold between irreducible representations (ir): $(B_{2g} + B_{3g}) \rightarrow E_g$; $A_u(C_2') \rightarrow A_{1u}$; $A_u(C_2') \rightarrow B_{1u}$; $B_{1u}(C_2') \rightarrow A_{2u}$ (see Appendix 3 of ref. 72).

†† The internuclear distance between $^{S}CM^{nn}$ is the same, independently of the surface Miller indexes: 2.556, 2.889, and 2.884 Å in Cu, Ag, and Au, respectively.[95]

‡‡ The complex herringbone reconstruction of Au(111) corresponds to a compressed atomic layer with an average lattice spacing of 2.76 Å along the [110] direction,[96] instead of the corresponding bulk plane value of 2.88 Å, despite the hexagonal symmetry is locally preserved. The Au(100) surface also bears a large cell reconstruction, resulting in a surface layer with an atomic density 25% larger than in the (100) bulk plane. The corresponding quasi-hexagonal surface layer displays an average interatomic spacing ($\sim$2.78 Å) very close to that of the (111)-herringbone reconstruction.[97,98] Finally, the Au(110) surface displays the renown (1 × 2) missing row reconstruction, which exhibits local (111) microfacets. The missing row reconstruction may be lifted by the adsorption of large heteroaromatic molecules like CuPc, which locally deconstructs the surface beneath the molecular scaffold.[99]

Table 2 MTPP (MPc) TSEAs (eV) of low-lying unoccupied SOs. Values of the highest TSEA are in bold[ab]

	$^{\sigma}a_{1g}$	$^{\sigma}b_{1g}$	$^{\pi}b_{2g}$	$^{\pi}e_{g}$	$^{pmc}e_{g}$	$^{pmc}b_{1u}$
VTPP	$0.66^{\downarrow}$	$0.31^{\uparrow}$	$0.01^{\downarrow}$	$\mathbf{2.23}^{\uparrow}$	$1.81^{\downarrow}$	$0.43^{\uparrow}$
VPc	$1.18^{\downarrow}$	$-0.95^{\uparrow}$	$0.53^{\downarrow}$	$\mathbf{2.94}^{\uparrow}$	$2.50^{\downarrow}$	$0.99^{\uparrow}$
CrTPP	$0.39^{\downarrow}$	$0.32^{\uparrow}$	$0.13^{\downarrow}$	$-0.37^{\downarrow}$	$\mathbf{1.76}^{\downarrow}$	$0.38^{\uparrow}$
CrPc	$1.13^{\downarrow}$	$-0.59^{\uparrow}$	$0.87^{\downarrow}$	$0.96^{\downarrow}$	$\mathbf{2.47}^{\downarrow}$	$0.97^{\uparrow}$
MnTPP	$-0.20^{\downarrow}$	$-3.59^{\downarrow}$	$-1.17^{\downarrow}$	$-1.57^{\downarrow}$	$\mathbf{1.33}^{\downarrow}$	$-0.09^{\uparrow}$
MnPc	$2.16^{\downarrow}$	$1.14^{\uparrow}$	$2.25^{\downarrow}$	$1.69^{\downarrow}$	$\mathbf{2.84}^{\downarrow}$	$0.93^{\uparrow}$
FeTPP	—	$0.41^{\uparrow}$	—	$0.71^{\downarrow}$	$\mathbf{1.85}^{\downarrow}$	$0.35^{\uparrow}$
FePc	—	$0.30^{\uparrow}$	—	$1.44^{\downarrow}$	$\mathbf{2.61}^{\downarrow}$	$0.95^{\uparrow}$
CoTPP	$\mathbf{2.13}^{\downarrow}$	$1.06^{\uparrow}$	—	—	$1.52^{\uparrow}$	$0.26^{\uparrow}$
CoPc	$\mathbf{3.00}^{\downarrow}$	$1.45^{\uparrow}$	—	—	$2.17^{\uparrow}$	$0.90^{\uparrow}$
NiTPP	—	$1.47^{\uparrow}$	—	—	$\mathbf{1.53}^{\uparrow}$	$0.27^{\uparrow}$
NiPc	—	$1.88^{\uparrow}$	—	—	$\mathbf{2.19}^{\uparrow}$	$0.91^{\uparrow}$
CuTPP	—	$1.35^{\downarrow}$	—	—	$\mathbf{1.61}^{\uparrow}$	$0.33^{\uparrow}$
CuPc	—	$1.78^{\downarrow}$	—	—	$\mathbf{2.25}^{\uparrow}$	$0.94^{\uparrow}$
ZnTPP	—	—	—	—	$\mathbf{1.64}^{\uparrow}$	$0.38^{\uparrow}$
ZnPc	—	—	—	—	$\mathbf{2.26}^{\uparrow}$	$0.96^{\uparrow}$

[a] HS MnTPP TSEA calculations have been run by adopting the B3LYP functional. [b] TSEA positive values correspond to the IE of the $MTPP^{-}$ (MPc^{-}) species; negative values indicate an unfavorable (costly) electron capture.

while those of the *n*s AOs centered on $^{S}_{B}CM^{nn}_{100}$ transform as the *ir*s a and b (see Fig. S15 of the ESI†) of the C_2 point group,[72] and simply correspond to the in-phase and out-of-phase linear combinations of the two *n*s AOs; (ii) SALCs of the *n*s AOs centered on $^{S}_{B}CM^{nn}_{110}$ and $^{S}_{H}CM^{nn}_{110}$ transform as the *ir*s a and b (see above); (iii) SALCs of the *n*s AOs centered on $^{S}_{T}CM^{nnn}_{111}$ are bases for the *ir*s a, b, and e (see Fig. S16 of the ESI†); SALCs of the *n*s AOs centered on $^{S}_{H}CM^{nn}_{111}$ transform as the *ir*s a and e (see Fig. S17 of the ESI†); SALCs of the *n*s AOs centered on $^{S}_{B}CM^{nn}_{111}$ are of symmetry a and b (see Fig. S15 of the ESI†).§§

3.3 MTPP and MPc chemisorbed on CM surfaces

The core of the present paper consists of providing a convincing molecular picture of the MTPP and MPc grafting to CM surfaces and then a local point of view of the substrate → adsorbate charge transfer, if present, by combining elementary symmetry and geometry arguments with readily accessible information about the unoccupied frontier electronic structure of the free adsorbates. Far from attempting a systematic analysis of the adsorption of all the MTPP and MPc herein considered on the different chemisorption sites present on CM(100), CM(110), and CM(111) surfaces, we will limit ourselves to focus on selected case studies for which (i) the adsorbate → substrate charge transfer is established and (ii) the structural perturbations undergone by the pmc upon adsorption are tiny.

3.3.1 VPc on Ag(111) and Au(111) surfaces. Despite lacking any literature data for the isolated VTPP, Eguchi *et al.* succeeded in characterizing VPc on Ag(111) by NEXAFS and XMCD.[100] The authors emphasized a wispy Ag(111) → VPc charge transfer and a flat orientation on the substrate.[100]

A few years ago, Mabrouk and Majewski[101] theoretically investigated the stability and the electronic and magnetic properties of VPc grafted to Au(111) by exploiting VASP.[102] The authors considered all the possible high-symmetry chemisorption sites reported in the bottom panel of Fig. 3 as well as different molecular orientations to conclude that the VPc chemisorption on Au(111) is weakly dependent on the adsorption site (the ΔE between the most (H_{fcc}) and least (T) stable sites amounts to 120 meV) and the substrate → adsorbate charge transfer is weak and quantifiable in 0.62 electrons.[101] Even without supercell periodic calculations and STM measurements, let us see how VPc ADF results combined with symmetry and geometrical considerations may provide useful insights into the grafting of VPc to Ag(111).

VPc TSEAs of the V 3d-based SOs are all but one positive (see Table 2 and Fig. 2); moreover, both the $^{\pi}e_g^{\uparrow}$ and $^{pmc}e_g^{\downarrow}$ TSEAs are very high (2.94 and 2.50 eV, respectively). In addition, the experimentally revealed role played by the VPc $^{\sigma}e_g$-like $^{\sigma}a_{1g}$ SO in the substrate → adsorbate charge transfer[100] necessarily implies the interaction of the V $3d_{z^2}$ AO with 5s ^{S}Ag SALCs transforming as the *ir* a in the chemisorption site local symmetry. As such, it can be useful to remember that the $^{\sigma}a_{1g}^{\downarrow}$ TSEA (1.18 eV; see Table 2 and Fig. 2) is significantly smaller than the $^{\pi}e_g^{\uparrow}$ and $^{pmc}e_g^{\downarrow}$ TSEAs (see above). Schematic representations of the 5s ^{S}Ag SALCs transforming as the *ir* a for the T, B, and H¶¶ sites are superimposed to the optimized ^{pmc}VPc placed at 2.8 Å‖‖ above the bulk terminated Ag(111) in Fig. 4 ($^{S}_{T}Ag^{nn}_{111}$–V, $^{S}_{B}Ag^{nn}_{111}$–V, and $^{S}_{H}Ag^{nn}_{111}$–V internuclear distances are 2.80, 3.15, and 3.26 Å, respectively).

Elementary symmetry, geometrical, and overlap considerations allow the following statements: (i) the participation of the VPc $^{\pi}e_g^{\uparrow}$ SOs to the $^{S}_{T}Ag^{nn}_{111}$ → VPc charge transfer is symmetry forbidden at the T site (see the 3D CPs displayed in Fig. 5); (ii) the contribution of the VPc $^{\pi}e_g^{\uparrow}$ SOs to the $^{S}_{T}Ag^{nnn}_{111}$ → VPc charge transfer should be very weak as the $^{S}_{T}Ag^{nnn}_{111}$–V internuclear distance is 4.02 Å; (iii) similarly weak should be the contribution of both the VPc $^{\pi}e_g^{\uparrow}$ and $^{pmc}e_g^{\downarrow}$ SOs (see Fig. 5) to the $^{S}_{H}Ag^{nn}_{111}$ → VPc charge transfer (the local C_3 symmetry of the H site is incompatible with the adsorbate local C_4 symmetry); (iv) both the VPc 3d-based $^{\sigma}e_g$-like $^{\sigma}a_{1g}^{\downarrow}$ (see Fig. 4) and $^{\pi}t_{2g}$-like $^{\pi}e_g^{\uparrow}$ (see Fig. 5) may effectively participate to the $^{S}_{B}Ag^{nn}_{111}$ → VPc charge transfer; (v) the VPc $^{pmc}e_g^{\uparrow}$ (see Fig. 5) is well tailored to participate to the $^{S}_{B}Ag^{nn}_{111}$/$^{S}_{B}Ag^{nnn}_{111}$ → VPc charge transfer (with VPc sitting at the B site, placed at 2.8 Å above the bulk-terminated Ag(111), and oriented as in Fig. 5, the $^{S}_{B}Ag^{nn}_{111}$–N^{Py} and $^{S}_{B}Ag^{nnn}_{111}$–N^{m} internuclear distances are almost identical (2.85 and 2.84 Å, respectively)). The VPc chemisorption B site, with V–N^{Py} bonds oriented along the [01$\underline{1}$] and [2$\underline{11}$] directions,

§§ The schematic representations of the CM(111) $^{S}_{T}CM^{nn}$ and $^{S}_{H}CM^{nn}$ *n*s AOs SALCs sketched in Fig. S16 and S17 (ESI†) do not consider the *n*s AOs normalization coefficients; the radii of the *n*s AOs localized on different $^{S}CM^{nn}$ are then the same. The interested reader may refer to Chapter 7 of ref. 72.

¶¶ Besides CM(111) T and B sites, two types of H sites characterize the surface: the H_{hcp} and the H_{fcc} in Fig. 3. If the attention is limited to the outermost CM(111) layer, H_{hcp} and H_{fcc} have the same environment.

‖‖ Blades *et al.* have thoroughly investigated the electronic and molecular properties of VCu_x^{+}, VAg_x^{+}, and VAu_x^{+} (x = 3, 14) clusters. The V–Ag bond distance varies between 2.76 Å (VAg_3^{+}) and 2.95 Å (VAg_{14}^{+}) with a mean value of 2.8 Å.[103]

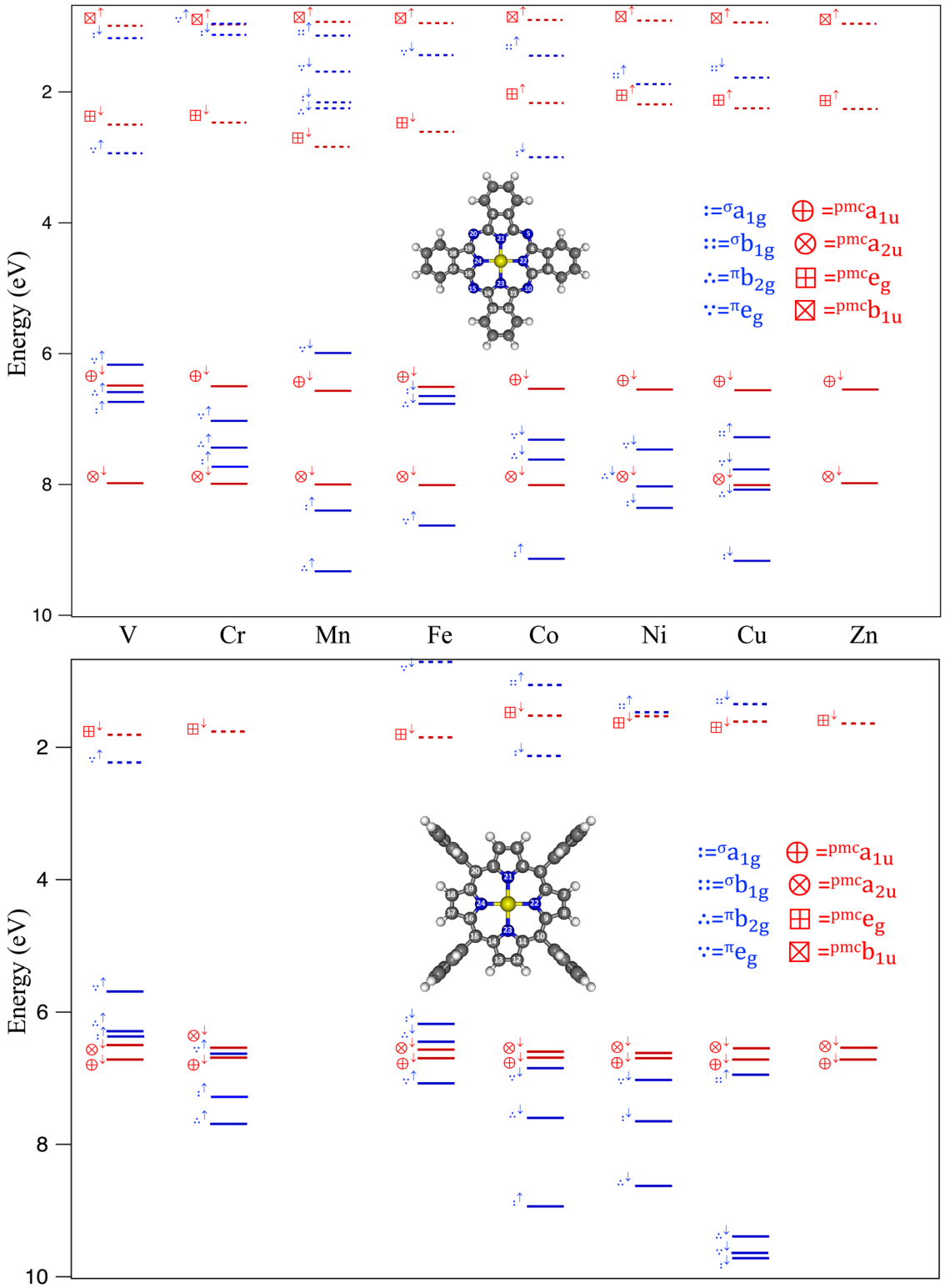

Fig. 2 TSIEs (solid lines) and TSEAs (dotted lines) of MPc and MTPP M 3d-based (blue lines) and $^{pmc}\pi$-based (red lines) spin orbitals. MnTPP TSIEs and TSEAs are not included in the figure, having been estimated by adopting the B3LYP[73,74,85] functional rather than the BP86 one[73,74] (see the main text).

seems then inescapable. This conclusion is only apparently in contrast with Mabrouk and Majewski[101] results because one must consider on one side the lower nobleness of Ag compared to Au ($^{Ag}\chi$ and $^{Au}\chi$ are 1.94 and 2.54 Pauling's units[65,66]) and, on the other side, the weak dependence on the adsorption site of the VPc chemisorption on Au(111). Results so far presented are

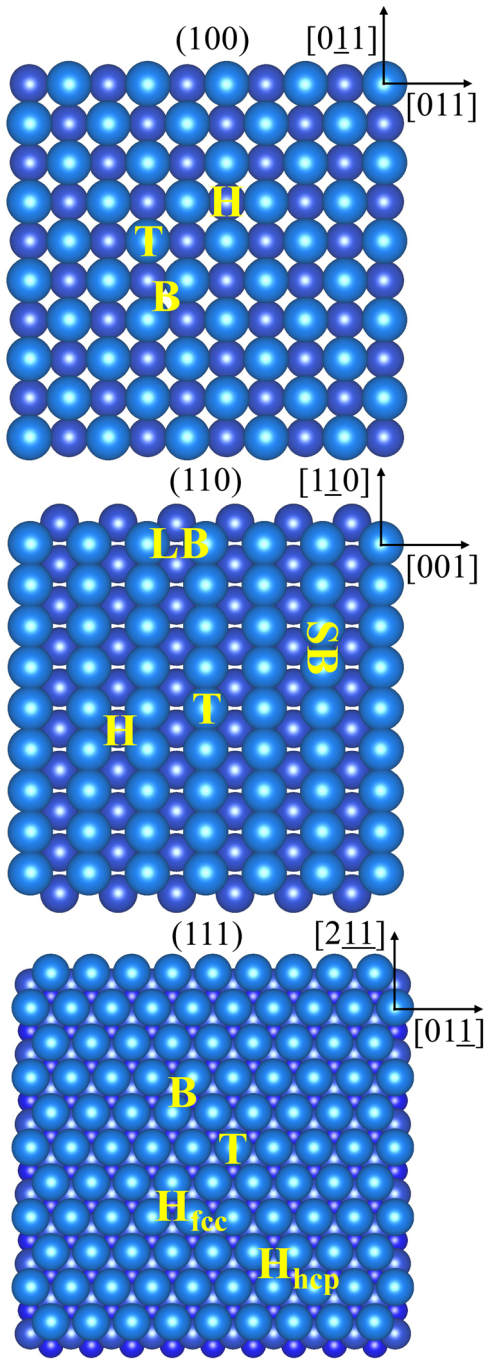

Fig. 3 Schematic representation of the high symmetry chemisorption sites (in yellow) on the CM(100), CM(110), and CM(111) bulk-terminated surfaces. T, B, and H stand for top, bridge, and hole, respectively. The topmost layer lies in the *XY* plane; moreover, the shades of blue correspond to different layers, with the most intense color corresponding to the deepest one.

useful to get information about the faint VPc species generated *in situ* on Ag(111),[100] and can be straightforwardly extended to other interfaces.

3.3.2 CoPc on CM surfaces. CoPc/CM(111) interfaces are particularly interesting because of the lack of a consensus about the nature and strength of the adsorbate–substrate interaction. Li *et al.*,[25] based on DFT numerical experiments, proposed a H_{hcp} chemisorption site (see Fig. 3) for CoPc on Ag(111) and Au(111) and the occupation of a B site for CoPc on Cu(111). These differences were ascribed to an adsorbate/substrate interaction significantly different upon moving from Cu(111) to Ag(111) and Au(111). In contrast, the experimental and theoretical outcomes gathered by Baran *et al.*[104,105] and Schmid *et al.*[106] for sub-ML of CoPc on Ag(111) prompted them to conclude that: (i) the CoPc chemisorption is accompanied by a spin state quenching from $S = \frac{1}{2}$ to $S = 0$; (ii) the Co 2p XPS features of the chemisorbed species shift towards lower binding energy consistently with an Ag(111) → CoPc charge transfer; (iii) the CoPc $^{\sigma}e_g$-like $^{\sigma}a_{1g}^{\downarrow}$ empty SO plays a leading role in determining the $Co^{II} \rightarrow Co^{I}$ reduction upon adsorption; (iv) the most stable chemisorption site corresponds to the T one with the Co^{II} species lying 2.90 ± 0.05 Å above the Ag(111) surface.[104,105] Interestingly, Zhao *et al.* reported similar evidence for CoPc on Au(111).[59]

As already stressed, the inspection of Table 2 and Fig. 2 indicates that: (i) the TSEAs of M 3d-based SOs exceed those of the $^{pmc}\pi^*$ ones only in the V and Co complexes; (ii) the CoPc $^{\sigma}e_g$-like $^{\sigma}a_{1g}^{\downarrow}$ TSEA has the highest value (3.00 eV) among those reported in the table and displayed in the figure. Moreover, Fig. 4 reveals at glance that $^{S}_{T}Ag^{nn}_{111}$ allows the best overlap between the Co^{II} $3d_{z^2}$ AO and the ^{S}Ag SALCs transforming as the *ir* a. The huge CoPc EA also makes possible the Au(111) → CoPc charge transfer (see above) despite the high $^{Au}\chi$ (2.54 Pauling's units[65,66]), while the different behavior of CoPc[59] (T site, large charge transfer) and VPc[101] (B site, weak charge transfer) on Au(111) may be reasonably traced back to (i) the fulfillment of CoPc $^{\pi}t_{2g}^{\uparrow}$-/$t_{2g}^{\downarrow}$-like SOs and (ii) the different TSEA of the $^{\sigma}e_g$-like $^{\sigma}a_{1g}^{\downarrow}$ in VPc and CoPc (see Table 2 and Fig. 2).

Results about the CoPc/Au(111) interface may be now exploited to shed new light into the CoPc/Au(110)[107] and CoPc/Au(100)[108,109] ones and for which the CoPc chemisorption site is still unknown. As such, it is experimentally established that the CoPc molecular plane lies parallel to the surface and results firmly anchored to the substrate both in CoPc/Au(110) and CoPc/Au(100);[107,108] moreover, NEXAFS at the Co $L_{2,3}$-edges and valence band photoemission suggested a reduction of the spin magnetic moment for CoPc/Au(110).[107] Photoemission studies of CoPc on Au(100) also demonstrate that the strong Au(100) → CoPc charge transfer determines the Co^{II} (d^7) → Co^{I} (d^8) surface reduction, most likely involving the Co-based $^{\sigma}e_g$-like $^{\sigma}a_{1g}^{\downarrow}$ SO, and then the quenching of the adsorbate magnetic moment ($S = 0$).[109] The giant CoPc first EA level (see Table 2 and Fig. 2) and the significant charge transfer from the Au(110) and Au(100) surfaces into the Co 3d-based SOs prompt us to indicate the T site as the most favorite not only for the CoPc chemisorption on Au(111) but also on Au(110) and Au(100). Concerning the azimuthal orientation of CoPc on Au(110), the inspection of Fig. 3 and 6 reveals that an effective substrate → adsorbate charge transfer involving the lowest-lying $^{pmc}\pi^*$ orbitals (the CoPc $^{pmc}e_g^{\uparrow}$ SOs TSEA = 2.17 eV; see Table 2 and Fig. 2) should imply the out-of-phase linear combination

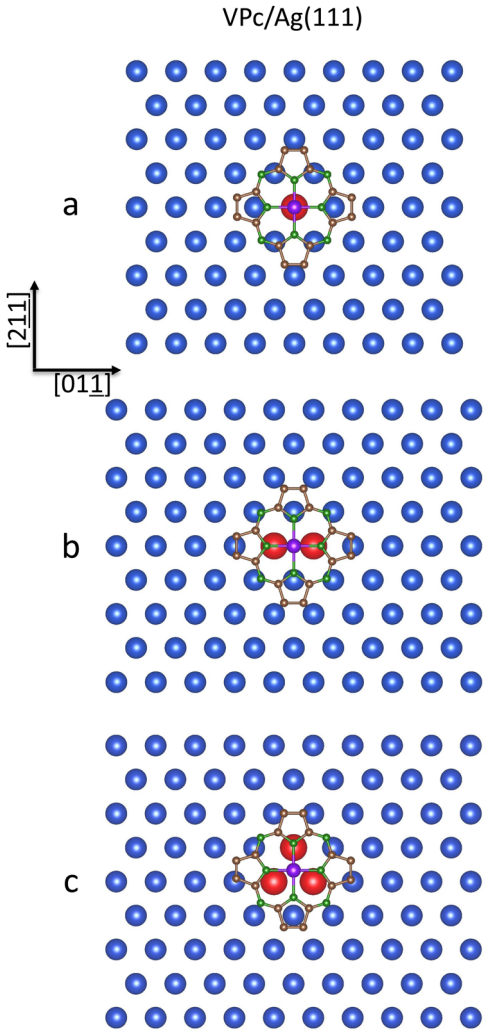

Fig. 4 Schematic representation of the ${}^{S}_{T}Ag^{nn}_{111}$ (a), ${}^{S}_{B}Ag^{nn}_{111}$ (b), and ${}^{S}_{H}Ag^{nn}_{111}$ (c) 5s AOs SALCs of symmetry a on the Ag(111) bulk-terminated surface superimposed to the optimized ^{pmc}VPc placed at 2.8 Å above the substrate and oriented with V–N^{Py} bonds aligned along the [211] and [011] directions. Only Ag(111) topmost layer atoms are displayed for clarity. Large red spheres represent $^{S}Ag^{nn}$ 5s AOs.

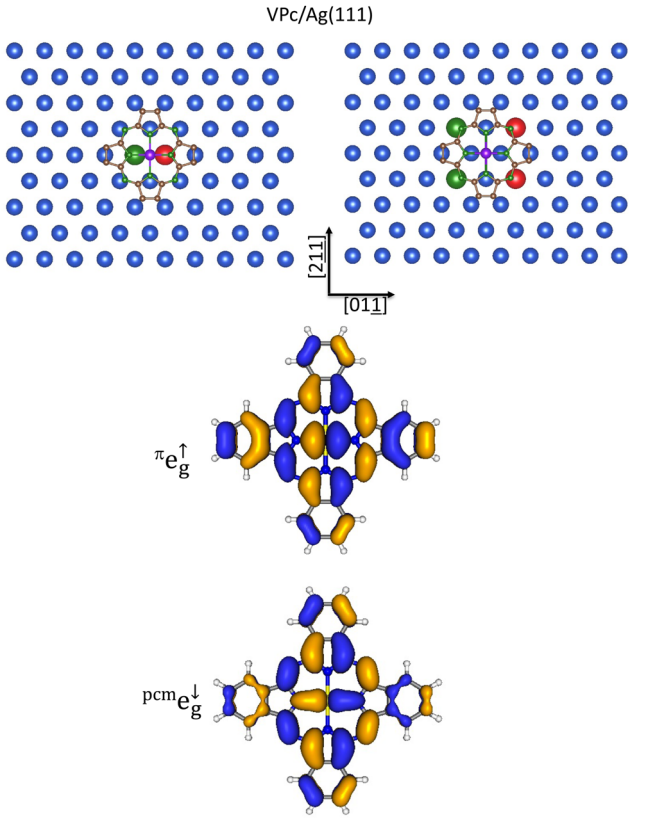

Fig. 5 Schematic representation of the ${}^{S}_{B}Ag^{nn}_{111}$ (upper left panel) and ${}^{S}_{B}Ag^{nnn}_{111}$ (upper right panel) 5s AOs SALC of symmetry b on the Ag(111) bulk-terminated surface superimposed to the optimized ^{pmc}VPc placed at 2.8 Å above the substrate and oriented with V–N^{Py} bonds aligned along the [211] and [011] directions. Only Ag(111) topmost layer atoms are displayed for clarity. Large spheres represent the $^{S}Ag^{nn}$ and $^{S}Ag^{nnn}$ 5s AOs, while different colors account for their different phases. 3D CPs of one component of the V^{II} $^{\pi}t_{2g}$-like $^{\pi}e_g^{\downarrow}$ SOs (middle panel) and one component of the $^{pmc}e_g^{\downarrow}$ π^* SOs (lower panel). Displayed isosurfaces correspond to ± 0.02 $e^{\frac{1}{2}}$ Å$^{-3/2}$ values.

of the ${}^{S}_{T}Au^{nnn}_{110}$ 6s AOs (see the upper panel of Fig. 6) and the CoPc $^{pmc}e_g^{\uparrow}$ SO having a node localized on the N^{Py} atoms aligned to the [001] direction (see the lower panel of Fig. 6). Incidentally, with the planar CoPc placed at 3 Å above the bulk-terminated Au(110) surface, the Co–${}^{S}_{T}Au^{nnn}_{110}$ and N^{Py}–${}^{S}_{T}Au^{nnn}_{110}$ internuclear distances are 4.16 and 3.15 Å, respectively.

For the Au(100) surface, the experimental evidence reported by Lindner *et al.*,[109] combined with the CoPc and CM(100) local fourfold symmetry, is also consistent with CoPc occupying a T site and the Co–N^{Py} bonds oriented along the [011] and [011] directions (see Fig. 3 and 7). As such, it is noteworthy that the chemisorption T site and the proposed orientation are best suited to favor the charge transfer from the ${}^{S}_{T}Au^{nn}_{100}$ 6s AO into the $^{\sigma}e_g$-like $^{\sigma}a_{1g}^{\downarrow}$ SO through a direct Co–${}^{S}_{T}Au^{nn}_{100}$ through-space interaction, which determines the experimentally detected Co^{II} (d^7) → Co^{I} (d^8) surface reduction.[109] Incidentally, the CoPc chemisorption at the Ag(100) H site, as proposed by Mugarza *et al.*,[110] is contradictory with the simultaneously reported charge transfer of one electron into the molecule; as such, it can be discarded.

The overlap between the SALCs of Au 6s AOs localized on the ${}^{S}_{T}Au^{nnn}_{100}$ and ${}^{S}_{T}Au^{nnnn}_{100}$, transforming as the *ir* e in the local C_4 symmetry, and the CoPc $^{pmc}e_g^{\uparrow}$ SO (see Fig. 7), provides a theoretical rationale for the tight anchoring of the adsorbate to the substrate. By the way, within the assumption of the CoPc molecular plane at 3 Å from the surface and the Co–N^{Py} bonds oriented along the [011] and [011] directions (see Fig. 7), the ${}^{S}_{T}Au^{nnn}_{100}$–N^{Py} and ${}^{S}_{T}Au^{nnnn}_{100}$–$N^{m}$ internuclear distances are 3.15 and 3.08 Å, respectively.

3.3.3 FePc on (100) and (110) CM surfaces. A planar arrangement of FePc was reported on both Au(110)[107] and Au(100) surfaces.[108] Moreover, Betti *et al.*[107] emphasized the quite strong bonding determined by the interaction of the Fe^{II} 3d-based AOs with the Au(110) surface.

The FePc $^{3}A_{2g}$ IS GS determined by the $[^{\sigma}a_{1g}^{\uparrow\downarrow}{}^{\pi}b_{2g\parallel}^{\uparrow\downarrow}{}^{\pi}e_{g\perp}^{\uparrow\uparrow}]$ configuration (see Table S14 of the ESI†) would prevent the

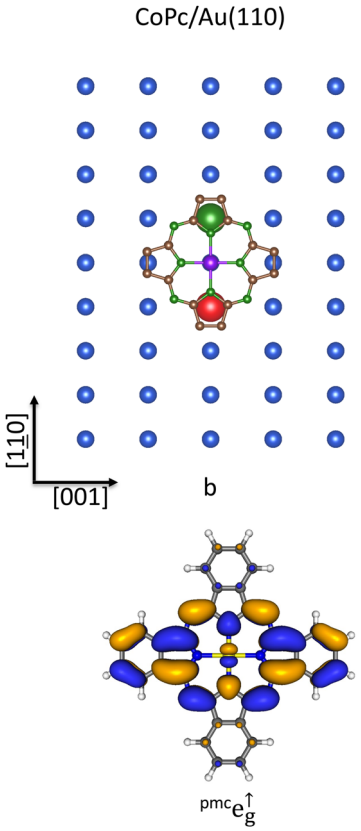

Fig. 6 Schematic representation of the ${}^{S}_{T}Au^{nnn}_{110}$ 6s AOs SALC of symmetry b on the Au(110) bulk-terminated surfaces superimposed to the optimized ^{pmc}CoPc placed at 3.0 Å above the substrate and oriented with Co–N^{Py} bonds aligned along the [1$\bar{1}$0] and [001] directions. Only Au(110) topmost layer atoms are displayed for clarity. Large spheres represent ${}^{S}_{T}Au^{nnn}_{110}$ 6s AOs, while different colors account for their different phases (upper panel). 3D CP of one component of the ${}^{pmc}e_g^{\uparrow}$ SOs (lower panel). Displayed isosurfaces correspond to ± 0.02 $e^{\frac{1}{2}}$ Å$^{-3/2}$ values.

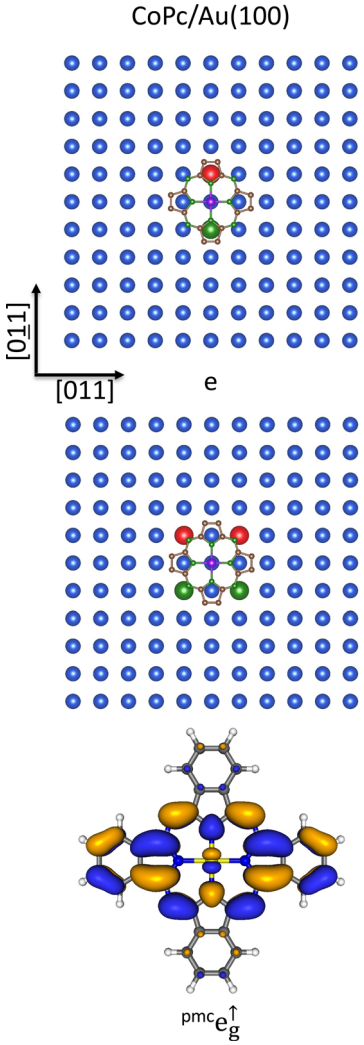

Fig. 7 Schematic representation of one component of the ${}^{S}_{T}Au^{nnn}_{100}$ (upper panel), ${}^{S}_{T}Au^{nnnn}_{100}$ (middle panel) 6s AOs SALC of symmetry e on the Au(100) bulk-terminated surface superimposed to the optimized ^{pmc}CoPc placed at 3.0 Å above the substrate and oriented with Co–N^{Py} bonds aligned to the [0$\bar{1}$1] and [011] directions. Only Au(100) topmost layer atoms are displayed for clarity. Large spheres represent ${}^{S}_{T}Au^{nnn}_{100}$ and ${}^{S}_{T}Au^{nnnn}_{100}$ 6s AOs, while different colors account for their different phases. 3D CP of one component of the ${}^{pmc}e_g^{\uparrow}$ SOs (lower panel). Displayed isosurfaces correspond to ± 0.02 $e^{\frac{1}{2}}$ Å$^{-3/2}$ values.

chemisorption site T because the antibonding component of the interaction between the completely occupied FePc ${}^{\sigma}e_g$-like ${}^{\sigma}a_{1g}^{\uparrow\downarrow}$ MO (the Fe^{II} $3d_{z^2}$-based MO) and the ${}^{S}_{T}Au^{nn}_{100}$ 6s AO would result partially occupied. Nevertheless, the minute ΔE between the FePc ${}^{3}E_g^{(1)}$ excited state generated by the $[{}^{\sigma}a_{1g\parallel}^{\uparrow\pi}b_{2g\perp}^{\uparrow\downarrow\pi}e_g^{\uparrow\uparrow\downarrow}]$ configuration and the ${}^{3}A_{2g}$ GS (47 meV; see Table S14 of the ESI†) must be kept in mind because tiny ligand field perturbations, for instance, those induced by chemisorption, could generate different occupation numbers of the Fe^{II} 3d-based SOs. As such, the TSEAs of the ${}^{3}E_g^{(1)}$ ${}^{\pi}t_{2g}$-like (${}^{\pi}_{\perp}e_g^{\downarrow}$) $12e_g$ LUMOs (3.04 eV) and ${}^{\sigma}e_g$-like (${}^{\sigma}a_{1g}^{\downarrow}$) $21a_{1g}$ LUMO+2 (2.70 eV), much higher than those reported in Table 2 for the low-lying empty SOs of the isolated molecule in its ${}^{3}A_{2g}$ GS, are consistent with a higher FePc electron-withdrawing capability in the ${}^{3}E_g^{(1)}$ state than in the ${}^{3}A_{2g}$ one. The ${}^{\pi}_{\perp}e_g^{\downarrow}$ and ${}^{\sigma}a_{1g}^{\downarrow}$ SOs bareness and their high TSEAs make them very well suited to actively participate to the substrate → adsorbate charge transfer and then to the anchoring of FePc to both Au(110) and Au(100).

Besides the abnormal gold nobleness[65,66] and the ${}^{3}E_g^{(1)}$ ${}^{\pi}_{\perp}e_g^{\downarrow}$ SOs TSEA (3.04 eV), higher than the ${}^{3}E_g^{(1)}$ ${}^{\sigma}a_{1g}^{\downarrow}$ one (2.70 eV), we may further account for the symmetry and geometry constraints to determine the FePc chemisorption site on Au(110). Starting with symmetry considerations: (i) the participation of the Fe^{II} ${}^{\pi}t_{2g}$-like ${}^{\pi}_{\perp}e_g^{\downarrow}$ SOs to the substrate → adsorbate charge transfer is symmetry forbidden for FePc chemisorbed at a T site of the Au(110) and Au(100) surfaces but symmetry allowed for FePc chemisorbed at the SB site in the former case and the B one in the latter (see Fig. 8);*** (ii) the participation of the Fe^{II} ${}^{\sigma}e_g$-like ${}^{\sigma}a_{1g}^{\downarrow}$ SO to the anchoring of FePc to both Au(110) and Au(100) is symmetry allowed for FePc chemisorbed

*** The Au(110) LB chemisorption site has not being herein considered because, with FePc positioned 2.85 Å above the bulk-terminated surface,[111] the Fe–${}^{S}_{LB}Ag^{nn}$ internuclear distance amounts to 3.504 Å.

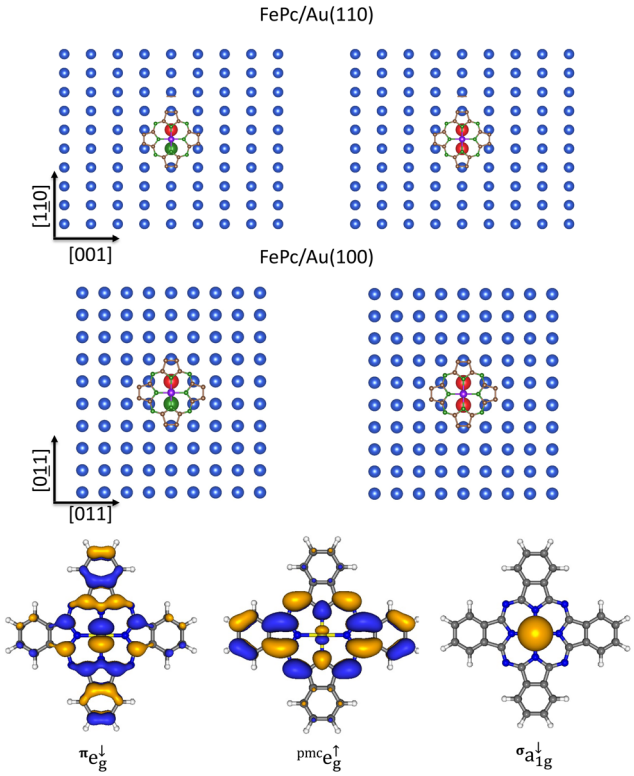

Fig. 8 Schematic representation of the ${}^{S}_{SB}Au^{nn}_{110}$ 6s AOs SALCs of symmetry b (upper, left panel) and a (upper, right panel) on the Au(110) bulk-terminated surface superimposed to the optimized ^{pmc}FePc placed at 2.85 Å above the substrate and oriented with Fe–N^{Py} bonds aligned to the [1$\bar{1}$0] and [001] directions. Only Au(110) topmost layer atoms are displayed for clarity. Large spheres represent ${}^{S}_{SB}Au^{nn}_{110}$ 6s AOs, while different colors account for their different phases. Schematic representation of the ${}^{S}_{B}Au^{nn}_{100}$ 6s AOs SALCs of symmetry b (middle, left panel) and a (middle, right panel) on the Au(100) bulk-terminated surface superimposed to the optimized ^{pmc}FePc placed at 2.85 Å above the substrate and oriented with Fe–N^{Py} bonds aligned to the [1$\bar{1}$0] and [011] directions. Only Au(100) topmost layer atoms are displayed for clarity. Large spheres represent ${}^{S}_{B}Au^{nn}_{100}$ 6s AOs, while different colors account for their different phases. 3D CPs of one component of the partially occupied FePc $^3E_g^{(1)}$ $^{\pi}t_{2g}$-like $^{\pi}e_g^{\downarrow}$ SOs (lower, left panel), unoccupied FePc $^3E_g^{(1)}$ $^{pmc}e_g^{\uparrow}$ π^* SOs (lower, middle panel), and unoccupied FePc $^3E_g^{(1)}$ $^{\sigma}a_{1g}^{\downarrow}$ SO (lower, right panel). Displayed isosurfaces correspond to ± 0.02 $e^{\frac{1}{2}}$ Å$^{-3/2}$ values.

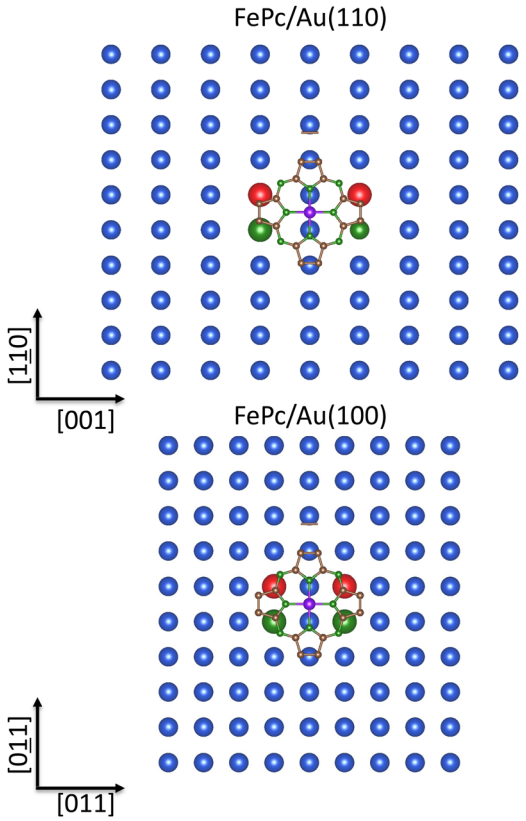

Fig. 9 Schematic representation of the ${}^{S}_{SB}Au^{nnn}_{110}$ and ${}^{S}_{B}Au^{nnn}_{100}$ 6s AOs SALCs of symmetry b on the Au(110) (upper panel) and Au(100) (lower panel) bulk-terminated surfaces superimposed to the optimized ^{pmc}FePc placed at 2.85 Å above the substrate and oriented with Fe–N^{Py} bonds aligned to the [1$\bar{1}$0] and [001] directions. Only Au(110) and Au(100) topmost layer atoms are displayed for clarity. Large spheres represent ${}^{S}_{SB}Au^{nnn}_{110}$ and ${}^{S}_{B}Au^{nnn}_{100}$ 6s AOs, while different colors account for their different phases.

at the SB site in the former case and the B one in the latter (see Fig. 8);*** (iii) the FePc $^{pmc}e_g$ π^* SOs (TSEA = 2.03 eV) may actively participate to the anchoring of FePc to both Au(110) and Au(100) when chemisorbed at the SB site in the former case and the B one in the latter. With specific reference to the third point, it has to be noted that the substrate → adsorbate charge transfer will involve different pmc atoms upon moving from the FePc/Au(110) interface to the FePc/Au(100) one (see Fig. 9).

From a geometry perspective, starting with FePc positioned 2.85 Å[111] above the bulk terminated Au(110) at the SB site*** (see Fig. 8 and 9), the ${}^{S}_{SB}Au^{nn}_{110}$–Fe, ${}^{S}_{SB}Au^{nn}_{110}$–N^{Py}, and ${}^{S}_{SB}Au^{nnn}_{110}$–$C^{\beta}$ internuclear distances are 3.19, 2.89, and 2.94 Å, respectively; moreover, with FePc positioned 2.85 Å[111] above the bulk terminated Au(100) at the B site (see Fig. 8 and 9), the ${}^{S}_{B}Au^{nn}_{100}$–Fe, ${}^{S}_{B}Au^{nn}_{100}$–N^{Py}, ${}^{S}_{B}Au^{nnn}_{100}$–C^{α}, and ${}^{S}_{B}Au^{nnn}_{100}$–N^{m} internuclear distances are 3.19, 2.89, 2.87, and 3.04 Å, respectively.

SALCs displayed in Fig. 9 and the 3D CP of the FePc $^{pmc}e_g^{\uparrow}$ π^* SOs (not herein reported because indistinguishable from the 3D CP of the CoPc $^{pmc}e_g^{\uparrow}$ π^* SOs reported in Fig. 7) allow us to assess that, for FePc at 2.85 Å[111] from the bulk terminated Au(110) and positioned at the SB site, the substrate → adsorbate charge transfer involving the $^{pmc}e_g^{\uparrow}$ π^* SOs will mainly concern the N^{Py} and C^{β} $2p_z$ AOs. For FePc at the same distance from the bulk terminated Au(100) and positioned at the B site, the substrate → adsorbate charge transfer involving the $^{pmc}e_g^{\uparrow}$ π^* SOs will mainly concern the N^{Py}, N^{m}, and C^{α} $2p_z$ AOs. The most stable chemisorption site of FePc on Au(110) and Au(100) should be then the SB and B one, respectively.

Strictly related to the just considered FePc/Au(110) interface, is the FePc/Ag(110) system; an interface able to catalyze the four-electron oxygen reduction reaction to form H_2O from O_2[46,112] and closely related to the oxygen-binding active center of hemoglobin. Some of us have thoroughly investigated the adsorbate–substrate interactions taking place at the FePc/Ag(110) interface through the combined use of high-resolution STM measurements and DFT supercell periodic calculations including semiempirical dispersion interactions.[111] Experimental measurements unveiled that FePc molecules result

parallel to the Ag(110) surface and arranged in rows running along the [001] direction (see the central panel of Fig. 3); moreover, two closely related phases (c(10 × 4) and p(10 × 4) superstructures) observed after depositing FePc at RT and persisting after extensive annealing at 473 K, were revealed at the sub-ML regime.

DFT calculations, indicated that: (i) chemisorption sites of the c(10 × 4) and p(10 × 4) superstructures are different, they correspond to T and SB sites, respectively, with a height of Fe^{II} with respect to the Ag(110) topmost layer of 2.85 Å in the c(10 × 4) phase and 2.54 Å in the p(10 × 4) one; (ii) in the c(10 × 4) phase, all the FePc molecules are oriented with their C_2' axes (those aligned with Fe–N^{Py} bonds) forming a 45° angle with the [1$\bar{1}$0] direction of the Ag substrate; (iii) in the p(10 × 4) phase, FePc molecules are arranged in an alternated sequence of two linear arrays, both aligned along the [001] direction of the Ag substrate and differing for the angle formed by their C_2' axes and the [1$\bar{1}$0] direction ((30 ± 2)° and (−30 ± 2)°, respectively).[111] Finally, even though the FePc IS state was mentioned, the authors provided no information about its symmetry.[111] All this evidence may be straightforwardly rationalized by referring, besides the symmetry and the geometry arguments invoked to assess the chemisorption site of FePc on Au(110), to the different $^{Au}\chi$ and $^{Ag}\chi$.[65,66] The $^{Ag}\chi$ value, significantly lower than the $^{Au}\chi$ one, and the high TSEA (2.70 eV) of the $^3E_g^{(1)}$ $^{\sigma}e_g$-like $^{\sigma}a_{1g}^{\downarrow}$ SO, concur to favor a direct Fe–Ag bonding interaction between the Fe^{II} $^{\sigma}e_g$-like $^{\sigma}a_{1g}^{\downarrow}$ and the $^{S}_{T}Ag^{nn}_{110}$ 5s AO and then a T chemisorption site. The FePc sitting at the T site does not prevent the possibility of an alternative chemisorption site, the SB one, with both the Fe^{II} $^{\pi}t_{2g}$-like $^{\pi}_{\perp}e_g^{\downarrow}$ and $^{\sigma}e_g$-like $^{\sigma}a_{1g}^{\downarrow}$ SOs contributing to the adsorbate–substrate grafting. We remark that the Fe atom optimized eight of 2.54 Å characterizing the p(10 × 4) phase[111] implies a $^{S}_{SB}Ag^{nn}_{110}$–Fe internuclear distance of 2.92 Å, very similar to the $^{S}_{T}Ag^{nn}_{110}$–Fe one (2.85 Å). Finally, the results herein reported for the FePc/Ag(110) interface can be straightforwardly transferred to the FePc/Cu(110) one.[113]

3.3.4 CoTPP and NiTPP on CM surfaces. The choice of CoTPP/CM and NiTPP/CM interfaces as two further case studies is determined by the evidence that, despite the huge amount of experimental and theoretical data available in the literature for CoTPP/Cu,[76,114–117] CoTPP/Ag,[76,114,117–122] CoTPP/Au,[76,115,118,120,123–125] NiTPP/Cu,[50,51,60,61,117] NiTPP/Ag,[117] and NiTPP/Au,[52,123] controversies about the actual MTPP adsorption geometry are still present. Starting from the Co^{II} tetrapyrroles, the following issues must be considered: (i) both Cu and Ag surfaces act as electron donors able to induce a Co^{II} (d^7) → Co^{I} (d^8) surface reduction,[114,115,118–121] while the Au substrate does not affect the Co oxidation state;[118,123,124] (ii) the Co^{II} (d^7) → Co^{I} (d^8) surface reduction,[114,115,118–121] systematically implies the fulfillment of the $^{\sigma}e_g$-like $^{\sigma}a_{1g}$ MO almost completely localized on the Co^{II} $3d_{z^2}$ AO and its concomitant loss of magnetization;[114] (iii) the CoTPP first affinity level corresponds to the Co $^{\sigma}e_g$-like $3d_{z^2}$-based $25a_{1g}^{\downarrow}$ SO (see Table 2 and Fig. 2); (iv) tiny differences in the chemisorption energy (∼85 meV) characterize different chemisorption sites on Ag(111).[119]

Experimentally, Schwarz *et al.*[126] ultimately stated the SB adsorption geometry and the adsorption height (2.25 ± 0.04 Å) of CoP on Cu(111) by combining STM, high-resolution XPS, XSW measurements, and DFT calculations. However, when TPPs are concerned, intermolecular interactions allowed by the rotational degrees of freedom of Ph fragment decorating the pmc may overcome those of M and pmc with the substrate. Some of us revealed by PED the coexistence of H_{hpc} and H_{fcc} sites for a saturated CoTPP layer on Ag(111), as driven by the Ph intercalation among adjacent molecules (the so-called T-type interaction).[127]

At first sight, the experimental and theoretical results collected by Schwarz *et al.*[126] are liable to affect the proposed approach; nevertheless, a thorough analysis of data reported in Table 2 and displayed in Fig. 2 demonstrates the opposite. The CoTPP highest TSEA (2.13 eV) is the largest among MTPP complexes (alike to CoPc among MPcs); however, it is noteworthy that the CoPc first affinity level (3.00 eV) significantly exceeds the CoTPP one. In addition, the TSEA of the CoTPP $^{\sigma}e_g$-like $3d_{x^2-y^2}$-based $13b_{1g}^{\downarrow}$ SO (1.06 eV), is the highest among lighter MTPP (ΔTSEA between CoTPP $^{\sigma}e_g$-like SOs = 1.07 eV). Incidentally, the ΔTSEA between the CoP $^{\sigma}e_g$-like SOs amounts to 1.00 eV.††† Now, the participation of the $^{\sigma}e_g$-like $3d_{x^2-y^2}$-based SO to the substrate → adsorbate charge transfer is prevented by symmetry when the adsorbate is chemisorbed at the T site, while the contribution of both $^{\sigma}e_g$-like MOs is symmetry allowed when the adsorbate occupies a B site (SB for the CM(110) surface). This is ultimately stated both experimentally and theoretically[126] for the least electronegative CM;[65,66] thus, it sounds reasonable that the chemisorption site of CoTPP on CM surfaces is, in the presence of a relevant substrate → adsorbate charge transfer involving the Co^{II} (d^7) → Co^{I} (d^8) reduction, the B one (SB for the CM(110)).

We recently addressed the adsorption configuration of NiTPP on Cu(100) by symmetry arguments as follows. The isolated NiTPP has a closed-shell nature and a $^1A_{1g}$ GS determined by the $^{\pi}t_{2g}{}^6$-$^{\sigma}e_g{}^2$-like configuration; moreover, the empty Ni^{II} 3d-based $^{\sigma}e_g$-like MO corresponds to the GS $12b_{1g}$ LUMO (see Fig. 10) whose TSEA (1.47 eV, see Table 2 and Fig. 2) is closely spaced to that of the $^{pmc}\pi^*$ $13e_g$ MOs (1.53 eV, see Table 2 and Fig. 2) and significantly higher than the TSEA of $9b_{1u}$ $^{pmc}\pi^*$ MO (the forth low-lying NiTPP empty orbital; see Table 2, Fig. 2, and Fig. 10).

Experimental and theoretical outcomes pertinent to the NiTPP/Cu(100) interface revealed that: (i) both the substrate and the adsorbate have a local C_4 symmetry;[128] (ii) the huge Cu(100) → NiTPP charge transfer taking place at the interface determines the partial occupation of all four low-lying unoccupied NiTPP MOs (the $^{\sigma}e_g$-like $12b_{1g}$, as well as the $13e_g$ and $9b_{1u}$ $^{pmc}\pi^*$ MOs; see Fig. 10);[128] (iii) the pmc of the chemisorbed NiTPP has a flat geometry,[128] it lies at 1.93 Å from the topmost layer of the surface,[60] and is characterized by the presence of the highly reactive $3d^9$ Ni^{I} species,[61] which excludes asorption at a T site by symmetry constraints.[60] With specific

††† The TSEA of the CoP $3d_{z^2}$-based $^{\sigma}a_{1g}^{\downarrow}$ and $3d_{x^2-y^2}$-based $^{\sigma}b_{1g}^{\uparrow}$ SOs are 1.73 eV and 0.73 eV, respectively.

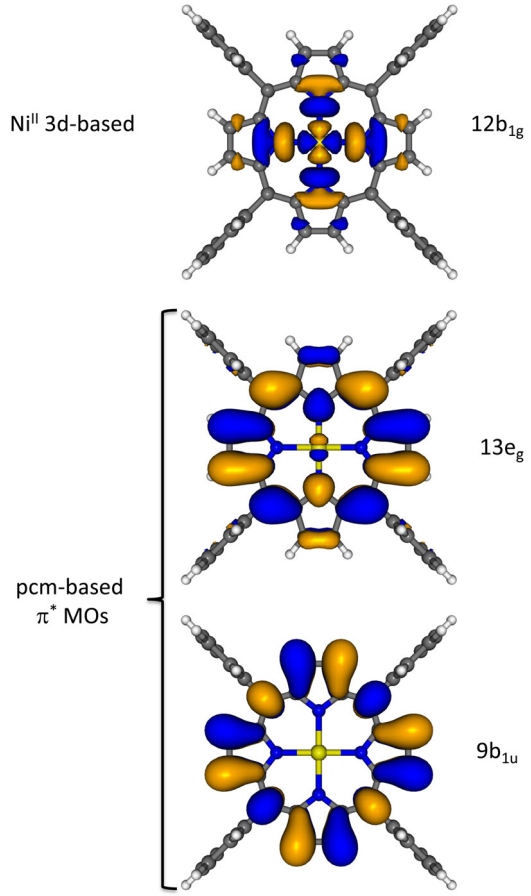

Fig. 10 3D CPs of low-lying NiTPP empty MOs (only one component of the $1\frac{3}{2}e_g$ orbital is reported); displayed isosurfaces correspond to ± 0.02 $e^{\frac{1}{2}}$ Å$^{-3/2}$ values.

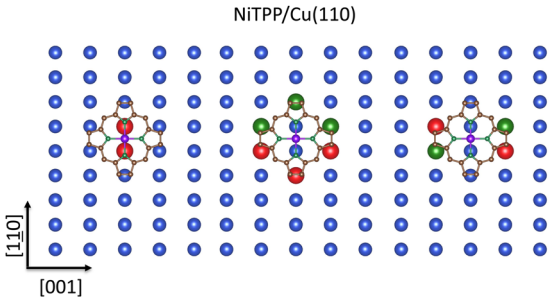

Fig. 11 Schematic representation of the ${}^{S}_{SB}Cu^{nn}_{110}$ 4s AOs SALC of symmetry a in the local C_2 symmetry of the Cu(110) bulk-terminate surface (left panel), ${}^{S}_{SB}Cu^{nnn}_{110}$ 4s AOs SALC of symmetry b in the local C_2 symmetry of the Cu(110) bulk-terminate surface (central panel), ${}^{S}_{SB}Cu^{nnn}_{110}$ 4s AOs SALC of symmetry a in the local C_2 symmetry of the Cu(110) bulk-terminate surface (right panel) superimposed to the optimized ^{pmc}NiTPP placed at 2 Å above the substrate and oriented with Ni–N^{Py} bonds aligned along the [1$\bar{1}$0] and [001] directions. Only Cu(110) topmost layer atoms are displayed for clarity. Large spheres represent ${}^{S}_{SB}Cu^{nn}_{110}$ and ${}^{S}_{SB}Cu^{nnn}_{110}$ 4s AOs, while different colors account for their different phases.

reference to the last point, the Ni^{II} ($3d^8$) → Ni^{I} ($3d^9$) surface reduction necessarily involves the only Ni^{II} 3d empty AO ($3d_{x^2-y^2}$), basis for the *ir* b in the local C_4 symmetry, whose overlap with the ${}^{S}_{T}Cu^{nn}_{100}$ 4s AO (basis for the *ir* a in the same fourfold symmetry) is identically zero. Thus, the substrate → adsorbed charge transfer rules the NiTPP adsorption on a specific chemisorption site; *i.e.*, the fourfold hollow site characterizing the Cu(100) surface (see the top panel of Fig. 3).[60] Incidentally, STM and STS results recently collected by Okuyama *et al.* indicate that CuPc (a single vacancy in the Cu^{II} $3d_{x^2-y^2}$) on Cu(100) maintains its flat geometry and occupies a C_4 H site.[129]

As far as the NiTPP/Cu(110) interface is concerned, MOT[130] results indicated a relevant adsorbate–substrate interaction characterized by a significant Cu(110) → NiTPP charge transfer and involving both the $13e_g$ and $9b_{1u}$ ${}^{pmc}\pi^*$ MOs of the isolated NiTPP. Zamborlini[117] also emphasized that, similarly to NiTPP/Cu(100), no contribution from the ${}^{\sigma}e_g$-like $12b_{1g}$ MO was revealed in the NiTPP/Cu(110) μ-ARPES maps. Incidentally, the absence of such a contribution in the NiTPP/Cu(100) μ-ARPES maps, successively revealed by NEXAFS measurements at the Ni L_3-edge,[61] was tentatively ascribed to the fact that the ${}^{\sigma}e_g$-like $12b_{1g}$ MO momentum map shows only four narrow lobes, presumably located outside the experimentally probed *k*-space range.[117]

To the best of the authors' knowledge, NEXAFS measurements at the Ni L_3-edge of the NiTPP/Cu(110) interface able to unequivocally determine the Ni oxidation state are not present in the literature. Nevertheless, it has been claimed that the Cu(110) → NiTPP charge transfer taking place at the NiTPP/Cu(110) interface is similar to that characterizing the NiTPP/Cu(100).[117] Thus the frontier electronic structure of the free NiTPP prevents a T chemisorption site and favors a SB site in agreement with periodic DFT calculations.[117] In fact, the empty Ni 3d-based MO reminiscent of the ${}^{\sigma}e_g$-like $12b_{1g}$ orbital may interact, in the local C_2 symmetry, with the ${}^{S}_{SB}Cu^{nn}_{110}$ 4s AOs SALC of symmetry a (see the left panel of Fig. 11). The inspection of Fig. 11, where the SALCs of symmetry b and a of the ${}^{S}_{SB}Cu^{nnn}_{110}$ 4s AOs are displayed in the central and right panels, makes evident that they are very well suited for transferring electronic charge into the ${}^{pmc}\pi^*$ MOs reminiscent of the free NiTPP $13e_g$ and $9b_{1u}$ orbitals, respectively.

The crystal structure shared by Cu and Ag, their very similar χ values (1.90 and 1.94 Pauling's units, respectively),[65,66] and the unoccupied frontier electronic structure of NiTPP would prompt to foresee the same SB chemisorption site for NiTPP/Cu(110) and NiTPP/Ag(110) interfaces, eventually imaging a weaker adsorbate–substrate interaction in the latter case determined by the larger size of Ag atoms (r_{Ag} = 1.60 Å) compared to that of the Cu ones (r_{Cu} = 1.35 Å).[65]

3.3.5 ZnTPP on CM surfaces. The last case study herein considered concerns the Zn^{II} tetrapyrroles/CM interfaces. The $3d^{10}$ closed shell configuration of the Zn^{II} ion carries with it both formal and substantial consequences. As far as the former is concerned, Zn^{II} tetrapyrroles are better described as complexes of a post-transition element (see IUPAC gold book definition);[131] on the other hand, the Zn^{II} configuration determines, even though indirectly, the chemisorption site of these

complexes on CM surfaces. More specifically, the substrate → adsorbate charge transfer, if present, can only involve the low-lying $^{pmc}\pi^*$ MOs as the interaction between the occupied $^{\pi}t_{2g}$-like/$^{\sigma}e_g$-like Zn^{II} 3d-based MOs and the ^{S}CM *n*s SALCs of suitable symmetry is repulsive in character. A sizable charge transfer and a tough substrate–adsorbate grafting of Zn^{II} tetrapyrroles to CM surfaces will then imply the minimization (maximization) of the interaction of the Zn^{II} 3d-based (low-lying $^{pmc}\pi^*$) MOs with ^{S}CM *n*s SALCs of suitable symmetry. The chemisorption T site on any CM surface will be ruled out because of the repulsive interaction between the Zn^{II} $^{\sigma}e_g$-like $^{\sigma}a_{1g}$ MO pointing directly toward the *n*s AO of symmetry a localized on the $^{S}_{T}CM^{nn}$. In addition, the inspection of the top panel of Fig. 3 reveals at glance that the CM(100) H site is also prevented because of the possible repulsive interaction between the Zn^{II} $^{\sigma}e_g$-like $^{\sigma}b_{1g}$ MO or, depending on the alignment of the chemisorbed pmc, $^{\pi}_{\parallel}t_{2g}$-like $^{\pi}b_{2g}$ MO and the CM *n*s SALC of symmetry b localized on $^{S}_{H}CM^{nn}$ (see Fig. S14 of the ESI†). The only possible chemisorption site of Zn^{II} tetrapyrroles on CM(100) should be then the B one. Moving to CM(111) substrates, the T site has already been excluded; moreover, the incompatibility of the local C_3 symmetry of the H site with the adsorbate local C_4 symmetry prevents the occupation of this site too. Again, the only possible chemisorption site of Zn^{II} tetrapyrroles on CM(111) should be the B one with Zn–N^{Py} bonds aligned with the [01$\bar{1}$] and [2$\bar{1}$1] directions.

The last substrate to be considered is the CM(110) one. Again, the inspection of Fig. 3 (middle panel) is enlightening. T and SB sites must be rejected because they are unfitted to minimize the repulsive interaction between Zn^{II} $^{\pi}t_{2g}$-like/$^{\sigma}e_g$-like completely occupied MOs and the underneath ^{S}CM atoms. As far as the CM(110) H and LB sites are concerned, a schematic representation of the Ag(110) with the optimized ^{pmc}ZnTPP placed at 2.8 Å[132] above the substrate and oriented with Zn–N^{Py} bonds aligned along the [1$\bar{1}$0] and [001] directions is reported in Fig. 12. The inspection of the figure reveals at once that the overlap between the $^{S}_{H}Ag^{nn}_{110}$ 5s SALC of symmetry b and the $13e_g$ $^{pmc}\pi^*$ MOs (see Fig. 10; NiTPP and ZnTPP 3D plots of the $13e_g$ MOs are indistinguishable) is poorer for the ^{pmc}ZnTPP at the H site than for the ^{pmc}ZnTPP at the LB one. In this regard, it must be mentioned that, with the ^{pmc}ZnTPP at 2.8 Å from the unreconstructed surface,[132] the shortest (longest) $^{S}_{H}Ag^{nn}_{110}$–N^{Py} internuclear distance is 3.15 Å (3.52 Å), while the $^{S}_{H}Ag^{nn}_{110}$–C^{m} and $^{S}_{H}Ag^{nn}_{110}$–C^{α} are 3.00 and 2.94 Å, respectively. At variance, N^{Py} atoms lying along the [001] direction are perfectly on top $^{S}_{LB}Ag^{nn}_{110}$ ($^{S}_{LB}Ag^{nn}_{110}$–N^{Py} internuclear distance is 2.80 Å); moreover, the $^{S}_{LB}Ag^{nnn}_{110}$–C^{m} and $^{S}_{LB}Ag^{nnn}_{110}$–C^{α} are 2.86 and 2.95 Å, respectively. In the presence of a significant substrate → adsorbate charge transfer, which, as already mentioned implies the maximization of the overlap between low-lying $^{pmc}\pi^*$ MOs and ^{S}CM *n*s SALCs of suitable symmetry, the favored CM(110) chemisorption site should be the LB one.

Available experimental evidence well agrees with the above-reported considerations. Baklanov *et al.*[132] investigated the adsorption configuration of ZnP on Cu(111) and Ag(111) by combining XSW, XPS, STM, bond-resolved AFM, LICAD, and DFT-based supercell periodic calculations (limited to the ZnP/Cu(111) interface) to conclude that the ZnP species chemisorbed on Cu(111) occupies the B site with two Zn–N^{Py} bonds oriented along the primary axis (see Scheme 1 of ref. 132). In addition, De Luca *et al.*,[133] based on STM and PES measurements on the ZnTPP/Au(111) interface, proposed the same B chemisorption site, superseding former claims of adsorption on T site.[134] Finally, Amsalem *et al.*[135] investigated the electronic and vibrational properties of the ZnPc/Ag(110) interface by LEED, STM, and HREELS measurements, whose outcomes were consistent with a quite strong substrate → adsorbate charge transfer, implying the partial filling of the ZnPc π^* LUMO. Amsalem *et al.*[135] also proposed a tentative model for the geometrical structure of 1 ML ZnPc/Ag(110), although arbitrarily placing the Zn^{II} ions on T and SB sites instead of the LB one.[135]

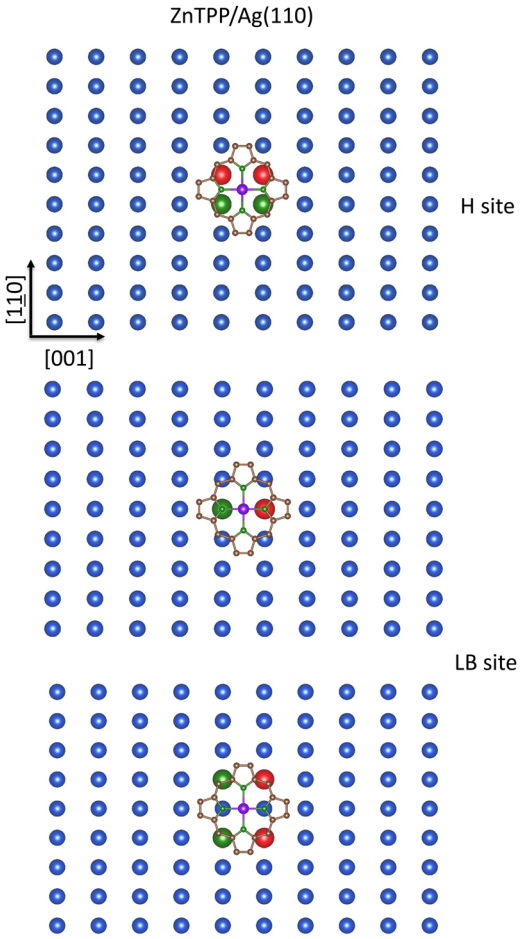

Fig. 12 Schematic representation of the $^{S}_{H}Ag^{nn}_{110}$ (upper panel), $^{S}_{LB}Ag^{nn}_{110}$ (middle panel), and $^{S}_{LB}Ag^{nnn}_{110}$ (bottom panel) 5s AOs SALCs transforming as the *ir* b in the local C_2 symmetry of the Ag(110) bulk-terminate surface superimposed to the optimized ^{pmc}ZnTPP placed at 2.8 Å above the substrate and oriented with Ni–N^{Py} bonds aligned along the [1$\bar{1}$0] and [001] directions. Only Ag(110) topmost layer atoms are displayed for clarity. Large spheres represent $^{S}Ag^{nn}$ and $^{S}Ag^{nnn}$ 5s AOs, while different colors account for their different phases.

4. Conclusions

Structural and electronic reasons determining a crystal field stronger in the Pc^{2-} ligand than in the TPP^{2-} one have been identified, and the impact of this difference on the frontier electronic structure of free MTPP and MPc (Z^M = 23–30; the largest series so far ever considered) has been investigated by DFT calculations with the ADF package. Easily accessible information about group 11 elements (crystal structure,[95] nobleness,[63] surface geometry[136]) combined with a thorough description of the free MTPP and MPc frontier electronic structure offer a cost-effective approach to foresee the chemisorption site of MTPP and MPc on low-index Cu, Ag, and Au surfaces, provided that two requirements are fulfilled: an established substrate → adsorbate charge transfer; the absence of significant distorsion of the macrocycle upon adsorption. A thorough comparison of the electronic structures of isolated MTPP and MPc and their building blocks indicates a more efficient substrate → adsorbate charge transfer in MPc than in MTPP. The stronger MPc ligand field, determined by the shrinking of the coordinative pocket and the higher π acceptor capability of MPc (see the ESI†), yields an overall electronegativity larger in MPc than in MTPP, which brings the MPc LUMOs closer in energy to the ^{S}CM SALCs. Because of their very similar electronegativities,[65,66] Cu and Ag surfaces show similar behaviors and predictable chemisorption sites, while the Au nobleness[63] prevents weighty charge transfer and only the chemisorption site of FePc (in its $^3E_g^{(1)}$ state) and CoPc on Au surfaces[59,137,138] may be shortly, easily, and cheaply foreseen. This information also provides an useful input to avoid time-expensive trial-and-error computations, when the full interfacial structural and electronic details details must be retrieved through costly numerical experiments. The predictive capability of the semi-quantitative approach herein proposed reinforces the idea that the adsorbate–substrate interaction, if strong, is a phenomenon mainly local in character[139] where the accuracy of the local description of the potential is more relevant than the inclusion of long-range effects and then it can be suitably treated through the molecular cluster approximation.[139–141]

Acronyms

ADF	Amsterdam density functional
AFM	Atomic force microscopy
AO	Atomic orbital
ARPES	Angular resolved photoelectron spectroscopy
ASPCS	Atomic subshell photoionization cross-sections
B	Bridge chemisorption site
B3LYP	Becke, 3-parameter, Lee–Yang–Parr
BP86	Becke–Perdew 86
CASPTn	Multi reference complete active space perturbation theory
CASSCF	Complete active space self-consistent field
CM	Coinage metal
C_n	Clockwise rotation through $\frac{2\pi}{n}$ radiants
CP	Contour plot
DFT	Density functional theory
DMRG	Density matrix renormalization group
DV-Xα	Discrete variational Xα
EA	Electron affinity
ESI	Electronic supplementary material
fcc	Face centered cubic
FMO	Frontier molecular orbital
GED	Gas phase electron diffraction
GGA	Generalized gradient approximation
GS	Ground state
H	Hollow chemisorption site
H_2P	Porphine
H_2Pc	Phthalocyanine
H_2Pz	Porphyrazine
H_2TPP	*meso*-Tetraphenylporphyrin
hcp	Hexagonal close packed
HOMO	Highest occupied molecular orbital
HREELS	High resolution electron energy loss spectroscopy
HS	High spin
i-Ind	Isoindole
IE	Ionization energy
IETS	Inelastic electron tunneling spectroscopy
IPS	Inverse photoemission spectroscopy
ir	Irreducible representation
IR	InfraRed
IS	Intermediate spin
IUPAC	Internation union of pure and applied chemistry
LB	Long bridge
LEED	Low energy electron diffraction
LICAD	Ligand-induced central atom displacement
LS	Low spin
LUMO	Lowest unoccupied molecular orbital
m	*meso*
M	Transition metal
ML	Monolayer
MO	Molecular orbital
MOT	Molecular orbital tomography
MP	Porphinato transition metal complex
MPc	Phthalocyaninato transition metal complex
MTPP	Tetraphenylporphirinato transition metal complex
n	Principal quantum number
NEXAFS	Near edge X-ray absorption fine structure
nn	Nearest neighbour
nnn	Next nearest neighbour
OEP^{2-}	2,3,7,8,12,13,17,18-Octaethylporphyrinato ion
OMTS	Orbital-mediated tunneling spectroscopy
P^{2-}	Porphinato ion
Pc^{2-}	Phthalocyaninato ion
PED	Photoelectron diffraction
PES	Photoelectron spectroscopy
Ph	Phenyl group
pmc	Planar aromatic macro cycle core
$PPhMe_2$	Dimethylphenyl phosphine
Py	Pyrrole
RASPT2	Multiconfigurational second-order perturbation theory restricted active space

RT	Room temperature
S	Total spin quantum number
SALC	Symmetry adapted linear combination
SB	Short bridge
^{S}CM	Surface coinage metal
SO	Spin orbital
STM	Scanning tunneling microscopy
STS	Scanning tunneling specroscopy
T	Top chemisorption site
TS	Transition state
TSEA	Transition state electron affinity
TSIE	Transition state ionization energy
THF	Tetrahydrofuran
TPP^{2-}	*meso*-Tetraphenyl porphirinato ion
TTP^{2-}	*meso*-Tetra-*p*-tolylporphyrinato ion
UV	Ultraviolet
VASP	Vienna *ab initio* Simulation Package
VdW	van der Waals
XC	Exchange–correlation
XMCD	X-Ray magnetic circular dichroism
XPS	X-Ray photoelectron spectroscopy
XSW	X-Ray standing wave
Z	Atomic number
χ	Electronegativity
μ	Magnetic moment
ν	Frequency
3D	Three dimensional

Author contributions

S. C.: investigation, data curation, writing – review & editing; I. C.: investigation, data curation, writing – review & editing; V. F.: investigation, data curation, writing – review & editing; L. S.: investigation, data curation, writing – review & editing; L. F.: investigation, data curation, writing – review & editing; M. C.: conceptualization, investigation, methodology, resources, supervision, writing original draft, writing – review & editing.

Data availability

The data supporting this article have been included as part of the ESI.†

Conflicts of interest

There are no conflicts to declare.

Notes and references

1 J. J. Davis, G. A. Orlowski, H. Rahman and P. D. Beer, *Chem. Commun.*, 2010, **46**, 54–63.
2 B. Schmaltz, T. Weil and K. Müllen, *Adv. Mater.*, 2009, **21**, 1067–1078.
3 W. Auwärter, K. Seufert, F. Bischoff, D. Ecija, S. Vijayaraghavan, S. Joshi, F. Klappenberger, N. Samudrala and J. V. Barth, *Nat. Nanotechnol.*, 2012, **7**, 41–46.
4 D. G. De Oteyza, J. M. García-Lastra, M. Corso, B. P. Doyle, L. Floreano, A. Morgante, Y. Wakayama, A. Rubio and J. E. Ortega, *Adv. Funct. Mater.*, 2009, **19**, 3567–3573.
5 W. R. Browne and B. L. Feringa, *Ann. Rev. Phys. Chem.*, 2009, **60**, 407–428.
6 J. Dintinger, S. Klein and T. W. Ebbesen, *Adv. Mater.*, 2006, **18**, 1267–1270.
7 P. Gambardella, S. Stepanow, A. Dmitriev, J. Honolka, F. M. F. de Groot, M. Lingenfelder, S. S. Gupta, D. D. Sarma, P. Bencok, S. Stanescu, S. Clair, S. Pons, N. Lin, A. P. Seitsonen, H. Brune, J. V. Barth and K. Kern, *Nat. Mater.*, 2009, **8**, 189–193.
8 D. Gatteschi, A. Cornia, M. Mannini and R. Sessoli, *Inorg. Chem.*, 2009, **48**, 3408–3419.
9 P. V. Bernhardt and G. A. Lawrance, *Comprehensive Coordination Chemistry II: Transition Metal Groups 9–12*, ed. D. E. Fenton, 2003, vol. 6.
10 D. L. Nelson, M. M. Cox and A. A. Hoskins, *Lehninger Principles of Biochemistry*, Freeman, W.H. Macmillan Learning, New York, NY, USA, 8th edn, 2021.
11 J. M. Berg, J. L. Tymoczko and L. Stryer, *Biochemistry*, W. H. Freeman, New York, NY, USA, 5th edn, 2002.
12 A. Tsuda and A. Osuka, *Science*, 2001, **293**, 79–82.
13 M. Planells, A. Forneli, E. Martínez-Ferrero, A. Sánchez-Díaz, M. A. Sarmentero, P. Ballester, E. Palomares and B. C. O'Regan, *Appl. Phys. Lett.*, 2008, **92**, 153506.
14 N. A. Rakow and K. S. Suslick, *Nature*, 2000, **406**, 710–713.
15 *The Porphyrin Handbook*, ed. K. M. Kadish, K. M. Smith and R. Guilard, Academic Press, New York, NY, USA, 2000.
16 J. Mack and M. J. Stillman, *The Porphyrin Handbook*, 2003, vol. 16, p. 43.
17 M. K. Engel, *The Porphyrin Handbook*, 2003, vol. 20, pp. 1–246.
18 C. Di Natale, D. Monti and R. Paolesse, *Mater. Today*, 2010, **13**, 46–52.
19 A. W. Hains, Z. Liang, M. A. Woodhouse and B. A. Gregg, *Chem. Rev.*, 2010, **110**, 6689–6735.
20 J. M. Gottfried, *Surf. Sci. Rep.*, 2015, **70**, 259–379.
21 J. M. Gottfried, *On-Surface Synthesis*, Springer, 2016.
22 Y.-f Geng, P. Li, J.-z Li, X.-m Zhang, Q.-d Zeng and C. Wang, *Coord. Chem. Rev.*, 2017, **337**, 145–177.
23 J. J. Ortiz-Garcia and R. C. R. C. Quardokus, *J. Vac. Sci. Technol., A*, 2023, **41**, 030801.
24 D. Dini and M. Hanack, *J. Porphyrins Phthalocyanines*, 2004, **8**, 915–933.
25 Z. Li, B. Li, J. Yang and J. G. Hou, *Acc. Chem. Res.*, 2010, **43**, 954–962.
26 A. B. Sorokin, *Chem. Rev.*, 2013, **113**, 8152–8191.
27 Q. Zhou, Z.-F. Liu, T. J. Marks and P. Darancet, *J. Phys. Chem. A*, 2021, **125**, 4055–4061.

28 M. Urbani, M.-E. Ragoussi, M. K. Nazeeruddin and T. Torres, *Coord. Chem. Rev.*, 2019, **381**, 1–64.
29 S. Keshipour and A. Asghari, *Int. J. Hydrogen Energy*, 2022, **47**, 12865–12881.
30 A. Galstyan, *Chem. – Eur. J.*, 2020, **27**, 1903–1920.
31 H. de Diesbach and E. von der Weid, *Helv. Chim. Acta*, 1927, **10**, 886–888.
32 I. M. Heilbron, F. Irving, R. P. Linstead and J. F. Thorpe (to Imperial Chemical Industries, Ltd.) British Patent 410814 (May 16, 1934).
33 R. B. Linstead, *J. Chem. Soc.*, 1934, 1016–1017.
34 C. E. Dent and R. B. Linstead, *J. Chem. Soc.*, 1934, 1027–1031.
35 R. B. Linstead and A. R. Lowe, *J. Chem. Soc.*, 1934, 1031–1033.
36 C. E. Dent, R. B. Linstead and A. R. Lowe, *J. Chem. Soc.*, 1934, 1033–1039.
37 P. A. Barrett, C. E. Dent and R. P. Linstead, *J. Chem. Soc.*, 1936, 1719–1736.
38 R. P. Linstead and J. M. Robertson, *J. Chem. Soc.*, 1936, 1736–1738.
39 M. A. Dahlen, *Ind. Eng. Chem.*, 1939, **31**, 839–847.
40 M. D. Angione, R. Pilolli, S. Cotrone, M. Magliulo, A. Mallardi, G. Palazzo, L. Sabbatini, D. Fine, A. Dodabalapur, N. Cioffi and L. Torsi, *Mater. Today*, 2011, **14**, 424–433.
41 S. H. Jang and A. K. Y. Jen, *Structured Organic Non-Linear Optics*, Academic Press, Amsterdam, 2011.
42 T. Nguyen, *Surf. Coat. Technol.*, 2011, **206**, 742–752.
43 W. Cao and J. Xue, *Energy Environ. Sci.*, 2014, **7**, 2123–2144.
44 B. Hulsken, R. Van Hameren, J. W. Gerritsen, T. Khoury, P. Thordarson, M. J. Crossley, A. E. Rowan, R. J. M. Nolte, J. A. A. W. Elemans and S. Speller, *Nat. Nanotechnol.*, 2007, **2**, 285–289.
45 K. S. Mali, N. Pearce, S. De Feyter and N. R. Champness, *Chem. Soc. Rev.*, 2017, **46**, 2520–2542.
46 F. Sedona, M. Di Marino, D. Forrer, A. Vittadini, M. Casarin, A. Cossaro, L. Floreano, A. Verdini and M. Sambi, *Nat. Mater.*, 2012, **11**, 970–977.
47 S. Carlotto, M. Sambi, F. Sedona, A. Vittadini, J. Bartolomé, F. Bartolomé and M. Casarin, *Phys. Chem. Chem. Phys.*, 2016, **18**, 28110–28116.
48 E. Bartolomé, J. Bartolomé, F. Sedona, J. Lobo-Checa, D. Forrer, J. Herrero-Albillos, M. Piantek, J. Herrero-Martín, D. Betto, E. Velez-Fort, L. M. García, M. Panighel, A. Mugarza, M. Sambi and F. Bartolomé, *J. Phys. Chem. C*, 2020, **124**, 13993–14006.
49 I. Cojocariu, S. Carlotto, H. M. Sturmeit, G. Zamborlini, M. Cinchetti, A. Cossaro, A. Verdini, L. Floreano, M. Jugovac, P. Puschnig, C. Piamonteze, M. Casarin, V. Feyer and C. M. Schneider, *Chem. – Eur. J.*, 2021, **27**, 3526–3535.
50 H. M. Sturmeit, I. Cojocariu, A. Windischbacher, P. Puschnig, C. Piamonteze, M. Jugovac, A. Sala, C. Africh, G. Comelli, A. Cossaro, A. Verdini, L. Floreano, M. Stredansky, E. Vesselli, C. Hohner, M. Kettner, J. Libuda, C. M. Schneider, G. Zamborlini, M. Cinchetti and V. Feyer, *Small*, 2021, **17**, 2104779.
51 I. Cojocariu, S. Carlotto, G. Zamborlini, M. Jugovac, L. Schio, L. Floreano, M. Casarin, V. Feyer and C. M. Schneider, *J. Mater. Chem. C*, 2021, **9**, 12559–12565.
52 I. Cojocariu, S. Carlotto, M. Jugovac, L. Floreano, M. Casarin, V. Feyer and C. M. Schneider, *J. Mater. Chem. C*, 2022, **10**, 9748–9757.
53 I. Cojocariu, S. Carlotto, D. Baranowski, M. Jugovac, J. Dreiser, L. Schio, L. Floreano, M. Casarin, V. Feyer and C. M. Schneider, *J. Mater. Chem. C*, 2023, **11**, 15521–15530.
54 P. Knecht, J. Reichert, P. S. Deimel, P. Feulner, F. Haag, F. Allegretti, M. Garnica, M. Schwarz, W. Auwärter, P. T. P. Ryan, T.-L. Lee, D. A. Duncan, A. P. Seitsonen, J. V. Barth and A. C. Papageorgiou, *Angew. Chem., Int. Ed.*, 2021, **60**, 16561–16567.
55 A. Basagni, L. Colazzo, F. Sedona, M. Di Marino, T. Carofiglio, E. Lubian, D. Forrer, A. Vittadini, M. Casarin, A. Verdini, A. Cossaro, L. Floreano and M. Sambi, *Chem. – Eur. J.*, 2014, **20**, 14296–14304.
56 I. Cojocariu, S. Carlotto, D. Baranowski, M. Jugovac, L. Schio, L. Floreano, M. Casarin, V. Feyer and C. M. Schneider, *Inorg. Chim. Acta*, 2023, **556**, 121657.
57 T. Furuyama, K. Satoh, T. Kushiya and N. Kobayashi, *J. Am. Chem. Soc.*, 2014, **136**, 765–776.
58 G. Raposo-Hernández, E. Sánchez Marcos, R. R. Pappalardo and J. M. Martínez, *J. Chem. Phys.*, 2023, **159**, 064110.
59 A. Zhao, Q. Li, L. Chen, H. Xiang, W. Wang, S. Pan, B. Wang, X. Xiao, J. Yang, J. G. Hou and Q. Zhu, *Science*, 2005, **309**, 1542–1544.
60 S. Carlotto, A. Verdini, G. Zamborlini, I. Cojocariu, V. Feyer, L. Floreano and M. Casarin, *Phys. Chem. Chem. Phys.*, 2023, **25**, 26779–26786.
61 G. Zamborlini, M. Jugovac, A. Cossaro, A. Verdini, L. Floreano, D. Lüftner, P. Puschnig, V. Feyer and C. M. Schneider, *Chem. Commun.*, 2018, **54**, 13423–13426.
62 M. Orchin and H. H. Jaffé, *Symmetry, Orbitals, and Spectra (S.O.S.)*, Wiley-Interscience, New York, 1971.
63 K. P. Kepp, *ChemPhysChem*, 2020, **21**, 360–369.
64 L. Pauling, *The nature of the chemical bond*, Cornel University, Ithaca, NY, 3rd edn, 1960, p. 88.
65 N. N. Greenwood and A. Earnshaw, *Chemistry of the Elements*, Butterworth-Heinemann, Cambridge, 2nd edn, 1984, p. 1176.
66 **https://www.webelements.com/periodicity/eneg_pauling/** reports $^{Cu}\chi$ = 1.90, $^{Ag}\chi$ = 1.93, and $^{Au}\chi$ = 2.54 Pauling's units.
67 P. Pyykkö and J.-P. Descalux, *Acc. Chem. Res.*, 1979, **12**, 276–281.
68 P. Pyykkö, *Chem. Rev.*, 1988, **88**, 563–594.
69 P. Pyykkö, *Angew. Chem., Int. Ed.*, 2004, **43**, 4412–4456.
70 A. J. Wallace, B. E. Williamson and D. L. Crittenden, *Can. J. Chem.*, 2016, **94**, 1163.
71 ADF2014, SCM, Theoretical Chemistry, Vrije Universiteit, Amsterdam, The Netherlands, **https://www.scm.com**.
72 B. E. Douglas and C. A. Hollingsworth, *Symmetry in Bonding and Spectra, an Introduction*, Academic Press, Orlando, FL, USA, 1985.

73 A. D. Becke, *Phys. Rev. A: At., Mol., Opt. Phys.*, 1988, **38**, 3098–3100.
74 J. P. Perdew, *Phys. Rev. B: Condens. Matter Mater. Phys.*, 1986, **33**, 8822–8824.
75 J. C. Slater, *Quantum Theory of Molecules and Solids. The Self-Consistent-Field for Molecules and Solids*, McGraw-Hill, New York, 1974, vol. 4.
76 S. Carlotto, I. Cojocariu, V. Feyer, L. Floreano and M. Casarin, *Nanomaterials*, 2022, **12**, 218.
77 G. Mangione, S. Carlotto, M. Sambi, G. Ligorio, M. Timpel, A. Vittadini, M. V. Nardi and M. Casarin, *Phys. Chem. Chem. Phys.*, 2016, **18**, 18727–18738.
78 G. Mangione, M. Sambi, S. Carlotto, A. Vittadini, G. Ligorio, M. Timpel, L. Pasquali, A. Giglia, M. V. Nardi and M. Casarin, *Phys. Chem. Chem. Phys.*, 2016, **18**, 24890–24904.
79 S. Carlotto, M. Sambi, F. Sedona, A. Vittadini and M. Casarin, *Nanomaterials*, 2021, **11**, 54.
80 S. Carlotto, M. Sambi, M. Rancan and M. Casarin, *Inorg. Chem.*, 2018, **57**, 1859–1869.
81 M. Casarin and S. Carlotto, *Eur. J. Inorg. Chem.*, 2018, 3145.
82 M. V. Nardi, F. Detto, L. Aversa, R. Verucchi, G. Salviati, S. Iannotta and M. Casarin, *Phys. Chem. Chem. Phys.*, 2013, **15**, 12864–12881.
83 G. Mangione, M. Sambi, M. V. Nardi and M. Casarin, *Phys. Chem. Chem. Phys.*, 2014, **16**, 19852–19855.
84 G. Mangione, L. Pandolfo, M. Sambi, G. Ligorio, M. V. Nardi, A. Cossaro, L. Floreano and M. Casarin, *Eur. J. Inorg. Chem.*, 2015, 2709–2713.
85 A. D. Becke, *J. Chem. Phys.*, 1993, **98**, 5648–5652.
86 C. A. Reed, J. K. Kouba, C. J. Grimes and S. K. Cheung, *Inorg. Chem.*, 1978, **17**, 2666–2670.
87 M.-S. Liao and S. Scheiner, *J. Chem. Phys.*, 2002, **117**, 205–219.
88 M.-S. Liao, J. D. Watts and M.-J. Huang, *J. Phys. Chem. A*, 2007, **111**, 5927–5935.
89 A. B. P. Lever, *J. Chem. Soc.*, 1965, 1821–1829.
90 M.-S. Liao and S. Scheiner, *J. Comput. Chem.*, 2002, **23**, 1391–1403.
91 M.-S. Liao and S. Scheiner, *J. Chem. Phys.*, 2001, **114**, 9780–9791.
92 K. A. Nguyen and R. Pachter, *J. Chem. Phys.*, 2001, **114**, 10757–10767.
93 J. F. Kirner, W. Dow and W. R. Scheidt, *Inorg. Chem.*, 1976, **15**, 1685–1690.
94 D. Nachtigallová, A. Antalík, R. Lo, R. Sedlák, D. Manna, J. Tucek, J. Ugolotti, L. Veis, O. Legeza, J. Pittner, R. Zboril and P. Hobza, *Chem. – Eur. J.*, 2018, **24**, 13413–13417.
95 **https://www.webelements.com/**.
96 S. B. Darling, A. W. Rosenbaum, Y. Wang and S. J. Sibener, *Langmuir*, 2002, **18**, 7462–7468.
97 D. Gibbs, B. M. Ocko, D. M. Zehner and S. G. J. Mochrie, *Phys. Rev. B: Condens. Matter Mater. Phys.*, 1990, **42**, 7330–7344.
98 D. L. Abernathy, D. Gibbs, G. Griibel, K. G. Huang, S. G. J. Mochrie, A. R. Sandy and D. M. Zehner, *Surf. Sci.*, 1993, **283**, 260–276.
99 L. Floreano, A. Cossaro, R. Gotter, A. Verdini, G. Bavdek, F. Evangelista, A. Ruocco, A. Morgante and D. Cvetko, *J. Phys. Chem. C*, 2008, **112**, 10794–10802.
100 K. Eguchi, T. Nakagawa, Y. Takagi and T. Yokoyama, *J. Phys. Chem. C*, 2015, **119**, 9805–9815.
101 M. Mabrouk and J. A. Majewski, *Comput. Theor. Chem.*, 2021, **1202**, 1133189.
102 G. Kresse and J. Furthmuller, *Phys. Rev. B: Condens. Matter Mater. Phys.*, 1996, **54**, 11169–11186.
103 W. H. Blades, A. C. Reber, S. N. Khanna, L. Lopez-Sosa, P. Calaminici and A. M. Köster, *J. Phys. Chem. A*, 2017, **121**, 2990–2999.
104 J. D. Baran, J. A. Larsson, R. A. J. Woolley, Y. Cong, P. J. Moriarty, A. A. Cafolla, K. Schulte and V. R. Dhanak, *Phys. Rev. B: Condens. Matter Mater. Phys.*, 2010, **81**, 075413.
105 J. D. Baran and J. A. Larsson, *J. Phys. Chem. C*, 2013, **117**, 23887–23898.
106 M. Schmid, A. Kaftan, H.-P. Steinrück and J. M. Gottfried, *Surf. Sci.*, 2012, **606**, 945–949.
107 M. G. Betti, P. Gargiani, R. Frisenda, R. Biagi, A. Cossaro, A. Verdini, L. Floreano and C. Mariani, *J. Phys. Chem. C*, 2010, **114**, 21638–21644.
108 O. V. Molodtsova, M. Knupfer, Yu. A. Ossipyan and V. Yu Aristov, *J. Appl. Phys.*, 2008, **104**, 083704.
109 S. Lindner, U. Treske, M. Grobosch and M. Knupfer, *Appl. Phys. A: Mater. Sci. Process.*, 2011, **105**, 921–925.
110 A. Mugarza, R. Roble, C. Krull, R. Korytar, N. Lorente and P. Gambardella, *Phys. Rev. B: Condens. Matter Mater. Phys.*, 2012, **85**, 155437.
111 M. Casarin, M. Di Marino, D. Forrer, M. Sambi, F. Sedona, E. Tondello, A. Vittadini, V. Barone and M. Pavone, *J. Phys. Chem. C*, 2010, **114**, 2144–2153.
112 J. H. Zagal, *Coord. Chem. Rev.*, 1992, **119**, 89–136.
113 R. A. Rehman, C. Y. Liang, Z. H. Jie, W. Ke, D. W. Dong, L. H. Yang, H. P. Mo and B. S. Ning, *Chin. Phys. B*, 2013, **22**, 063101.
114 T. Houwaart, T. Le Bahers, P. Sautet, W. Auwärter, K. Seufert, J. V. Barth and M. L. Bocquet, *Surf. Sci.*, 2015, **635**, 108–114.
115 A. Weber-Bargioni, W. Auwärter, F. Klappenberger, J. Reichert, S. Lefrançois, T. Strunskus, C. Wöll, A. Schiffrin, Y. Pennec and J. V. Barth, *ChemPhysChem*, 2008, **9**, 89–94.
116 P. Donovan, A. Robin, M. S. Dyer, M. Persson and R. Raval, *Chem. – Eur. J.*, 2010, **16**, 11641–11652.
117 G. Zamborlini, *Organic-Metal Hybrid Interfaces at the Mesoscopic Scale*, Forschungszentrum Jülich GmbH, Zentralbibliothek, Verlag, 2018.
118 J. M. Gottfried and H. Marbach, *Z. Phys. Chem.*, 2009, **223**, 53–74.
119 W. Hieringer, K. Flechtner, A. Kretschmann, K. Seufert, W. Auwärter, J. V. Barth, A. Görling, H. P. Steinrück and J. M. Gottfried, *J. Am. Chem. Soc.*, 2011, **133**, 6206–6222.

120 T. Lukasczyk, K. Flechtner, L. R. Merte, N. Jux, F. Maier, J. M. Gottfried and H. P. Steinrück, *J. Phys. Chem. C*, 2007, **111**, 3090–3098.
121 D. Wechsler, M. Franke, Q. Tariq, L. Zhang, T. L. Lee, P. K. Thakur, N. Tsud, S. Bercha, K. C. Prince, H. P. Steinrück and O. Lytken, *J. Phys. Chem. C*, 2017, **121**, 5667–5674.
122 W. Auwärter, K. Seufert, F. Klappenberger, J. Reichert, A. Weber-Bargioni, A. Verdini, D. Cvetko, M. Dell'Angela, L. Floreano, A. Cossaro, G. Bavdek, A. Morgante, A. P. Seitsonen and J. V. Barth, *Phys. Rev. B: Condens. Matter Mater. Phys.*, 2010, **81**, 245403.
123 L. Scudiero, D. E. Barlow and K. W. Hipps, *J. Phys. Chem. B*, 2000, **104**, 11899–11905.
124 K. W. Hipps and U. Mazur, *J. Porphyrins Phthalocyanines*, 2012, **16**, 1–9.
125 D. E. Barlow, L. Scudiero and K. W. Hipps, *Langmuir*, 2004, **20**, 4413–4421.
126 M. Schwarz, M. Garnica, D. A. Duncan, A. P. Paz, J. Ducke, P. S. Deimel, P. K. Thakur, T.-L. Lee, A. Rubio, J. V. Barth, F. Allegretti and W. Auwaïter, *J. Phys. Chem. C*, 2018, **122**, 5452–5461.
127 W. Auwärter, K. Seufert, F. Klappenberger, J. Reichert, A. Weber-Bargioni, A. Verdini, D. Cvetko, M. Dell'Angela, L. Floreano, A. Cossaro, G. Bavdek, A. Morgante, A. P. Seitsonen and J. V. Barth, *Phys. Rev. B: Condens. Matter Mater. Phys.*, 2010, **81**, 245403.
128 G. Zamborlini, D. Lüftner, Z. Feng, B. Kollmann, P. Puschnig, C. Dri, M. Panighel, G. Di Santo, A. Goldoni, G. Comelli, M. Jugovac, V. Feyer and C. M. Schneider, *Nat. Commun.*, 2017, **8**, 1–8.
129 H. Okuyama, S. Kuwayama, Y. Nakazawa, S. Hatta and T. Aruga, *Surf. Sci.*, 2022, **723**, 122126.
130 P. Puschnig, S. Berkebile, A. J. Fleming, G. Koller, K. Emtsev, T. Seyller, J. D. Riley, C. Ambrosch-Draxl, F. P. Netzer and M. G. Ramsey, *Science*, 2009, **326**, 702–706.
131 **https://doi.org/10.1351/goldbook.T06456**.
132 A. Baklanov, J. T. Küchle, D. A. Duncan, P. T. P. Ryan, R. J. Maurer, M. Schwarz, E. C. Rascon, I. Piquero-Zulaica, H. T. Ngo, A. Riss, F. Allegretti and W. Auwärter, *J. Phys. Chem. C*, 2023, **127**, 7501–7512.
133 O. De Luca, T. Caruso, I. Grimaldi, A. Policicchio, V. Formoso, J. Fujii, I. VoborniK, D. Pacilé, M. Papagno and R. G. Agostino, *Nanotechnology*, 2020, **31**, 365603.
134 C. Ruggieri, S. Rangan, R. A. Bartynski and E. Galoppini, *J. Phys. Chem. C*, 2015, **119**, 6101–6110.
135 P. Amsalem, L. Giovanelli, J. M. Themlin and T. Angot, *Phys. Rev. B: Condens. Matter Mater. Phys.*, 2009, **79**, 235426.
136 A. Zangwill, *Physics at Surfaces*, Cambridge University Press, Cambridge, 1996.
137 L. Massimi, M. Angelucci, P. Gargiani, M. G. Betti, S. Montoro and C. Mariani, *J. Chem. Phys.*, 2014, **140**, 244704.
138 M. G. Betti, P. Gargiani, R. Frisenda, R. Biagi, A. Cossaro, A. Verdini, L. Floreano and C. Mariani, *J. Phys. Chem. C*, 2010, **114**, 21638–21644.
139 M. Casarin, C. Maccato and A. Vittadini, *J. Phys. Chem. B*, 1998, **102**, 10745–10752.
140 M. Casarin, G. Granozzi, M. Sambi, E. Tondello and A. Vittadini, *Surf. Sci.*, 1994, **307–309**, 95–100.
141 M. Casarin, C. Maccato and A. Vittadini, *J. Chem. Soc., Faraday Trans.*, 1998, **94**, 797–804.